Large-scale two-photon imaging of living mouse brain utilizing hydrophilized fluoropolymer nanosheet

Takahashi, Taiga

Doctor of Philosophy

The Graduate University for Advanced Studies, SOKENDAI
School of Life Science
Department of Physiological Sciences

National Institute for Physiological Sciences
Division of Biophotonics

INDEX

Summary

In vivo imaging using two-photon microscopy in animal brains with a broad field of view reveals the functional connectivity between brain regions. To observe mouse brains, the “open skull method” creates a cranial window in which a portion of the mouse skull is completely removed and replaced with a high transparent material such as a glass coverslip. However, bleeding at the brain surface is inevitable when removing the submillimeter-thick cranial skull. This, in turn, results in the deterioration of fluorescent signals from the optical absorption of hemoglobin. In addition, the open skull method usually provides a small cranial window (2 - 4 mm in diameter) to avoid injury in large vessels and unnecessary bleeding. Generally, the size of cranial windows using a flat glass coverslip is restricted to a maximum diameter of 5 mm to avoid pressure on the brain tissue. To overcome this size restriction, methods with large cranial windows have been proposed that use novel sealing materials such as curved-glass or soft-polymer. These methods can avoid pressure on the brain surface because the sealing materials are designed to fit the curvature of the living brain surface. Unfortunately, these sealing materials are thick with high refractive indices, resulting in various optical aberrations.

In this study, I propose a novel cranial window approach utilizing thin polymer film, also known as a nanosheet, as a sealing material for *in vivo* two-photon imaging with a broad field of view (FOV). Nanosheets at approximately 10–100-nm thickness has unique properties, including high adhesion strength, flexibility, and transparency. Previously, biocompatible nanosheets composed of poly (L-lactic acid) were developed as glue-free wound dressing to efficiently stop bleeding of organs such as the liver and skin.

To apply a nanosheet to a living mouse brain, I used a polyethylene-oxide coated

CYTOP (PEO-CYTOP) nanosheet with a thickness of ~130 nm. I chemically hydrophilized a single-side surface of the sheet through modification with polyethylene oxide (PEO) to reduce inflammatory reactions. As a sealing material for cranial windows in the open skull method, PEO-CYTOP nanosheets were confirmed to firmly adhere to brain surfaces resulting in the suppression of bleeding from superficial veins. Next, using the flexibility of PEO-CYTOP nanosheets, I successfully made a large cranial window approximately the size of the whole parietal region. The window allowed for *in vivo* two-photon imaging of neural structure with a broad FOV at a high spatial resolution on the parietal region of Thy1-EYFP-H transgenic mice. To demonstrate wide-field imaging on the whole parietal region, I used Ca^{2+} imaging by epi-fluorescent microscopy in the G7NG817 transgenic mouse expressing a Ca^{2+} indicator G-CaMP7 primarily in astrocytes. To verify long-term availability, a small cranial window with a PEO-CYTOP nanosheet was covered with a glass coverslip to protect the brain surface against foreign substances and injury. Up to 9 weeks after the initial surgery, the transparency of the cranial window was maintained. Importantly, *in vivo* two-photon Ca^{2+} imaging at a single-cell resolution was achieved through the cranial window of G7NG817 transgenic mice at this time point.

Furthermore, I improved the cranial window method by combining the PEO-CYTOP nanosheet with UV curable resin (NIRE, Nanosheet Improved by light curable REsin). In this method, I laminated UV curable resin on the upper surface of the PEO-CYTOP nanosheet to seal the cranial window. During resin curing by UV irradiation, harmful heat production was suppressed by optimizing the irradiation time and light power with a handmade programmable UV irradiation system. As a result, the NIRE method successfully allowed for visualization of various neural structures in multi-scale ranging

from the whole parietal region to single dendritic spines of a neuron in the Thy1-EYFP-H transgenic mouse. Furthermore, the NIRE method facilitated *in vivo* multi-scale Ca^{2+} imaging for neural activities from a population of several hundred neurons to single dendritic spines in jGCaMP7 expressing mouse brains. In addition, this method suppressed motion artifacts. Notably, the cranial window maintained transparency for over 166 days, likely due to the suppression of inflammatory reactions. Finally, the NIRE method successfully demonstrated *in vivo* 3D imaging of Thy1-EYFP-H transgenic mice through such a large cranial window from the cerebral cortex to the cerebellum.

In conclusion, I utilized a PEO-CYTOP nanosheet as a sealing material for cranial windows to achieve *in vivo* imaging with a broad FOV in the mouse brain. I also proposed the NIRE method to achieve *in vivo* multi-scale and long-term imaging of neural structures and neural activities in mouse brains. This method promotes the understanding of brain functions based on the coordinated activities across multiple cortical regions in living animals.

Introduction

In vivo two-photon imaging

Large-scale measurements in the living brains of animals have been used to reveal the anatomical and functional connectivity between brain regions and their underlying functions [1], [2]. *In vivo* two-photon microscopy visualizes neural activities and ensembles in living mammalian brains across multiple regions at a sub-cellular resolution [3]–[7].

In two-photon microscopy, a single fluorescent molecule simultaneously absorbs two photons during two-photon excitation. Because the wavelength is inversely proportional to the energy of the photon, the wavelength required for two-photon excitation is nearly twice that of one-photon excitation. The near-infrared laser light pulses typically employed for two-photon excitation are less scattered and absorbed than in the excitation of visible light. Thus, two-photon microscopy is particularly useful for observing deeper regions of the living brain [8]–[10]. Additionally, out-of-focus excitation resulting in undesired fluorescent signals occurs less in two-photon microscopy because the fluorescence signal is generated only at the focal spot of the objective lens, unlike confocal microscopy. The localized excitation of two-photon excitation can also minimize photobleaching and photodamage during the observation of living tissues.

To facilitate *in vivo* imaging of multiple regions in the animal brain by *in vivo* two-photon microscopy, various techniques have been developed. These include: utilizing a high-power laser [11]–[13], an objective lens with a high numerical aperture (NA) and low magnification [14]–[17], optic devices[18]–[21], and multiplexing of laser pathways [14], [15], [22]–[25]. The number of detectable neurons using two-photon microscopy

tends to significantly each year [26], [27].

Cranial Window

For *in vivo* imaging of mouse brains using two-photon microscopy, the “thinned-skull method” and the “open skull method” are employed to create the cranial window. In the thinned-skull method, the cranial window is made by thinning the skull to a thickness of 10–15 μm without removal of the skull [28], [29]. Thus, the thinned-skull method is minimally invasive but requires thinning the skull repeatedly to keep the transparency of the cranial window for the long term because of bone regrowth [29]. In addition, the thinned-skull window cannot visualize microstructures, especially in the deep regions of the living mouse brain due to the residual skull. To improve the optical transparency, optical clearing techniques have been proposed for this method [30], [31]. However, these techniques do not always allow *in vivo* imaging at sub-cellular resolution because the transparency of the cranial window is dependent on the surgical procedure. Furthermore, bone regrowth is also inevitable in long-term observation.

On the other hand, the open skull method enables *in vivo* imaging of mouse brains at high resolution, especially in deep regions. In the open skull method, the cranial window is usually made by removing a part of the skull and sealing the cranial hole with a glass coverslip [32], [33]. Contrary to the thinned-skull method, a portion of the mouse skull is completely removed and replaced with highly transparent material. This method is used to achieve long-term imaging of the living mouse brain at high resolution. However, bleeding at the brain surface during this method is inevitable because of the surgery to remove the submillimeter-thick cranial skull. The surface bleeding of the brain deteriorates fluorescent signals and optically accessible depth due to the optical

absorption of hemoglobin. With long-term observation, the regrowth and thickening of the dura also deteriorate the optical transparency of the cranial windows. In addition, it is more challenging to make cranial windows on the superior sagittal sinus and transverse sinus because these cavities bleed easily and re-bleeding frequently occurs. Generally, the cranial window using the open skull method is small (2 - 4 mm in diameter) to avoid the removal of the skull on large vessels and any unnecessary bleeding. In addition, the size of the cranial windows is typically restricted to 5 mm in diameter to avoid the pressure on the brain tissue by a flat glass coverslip [34].

To overcome the limitation of scale, novel methods have been proposed for enlarging the size of the cranial window, such as curved-glass or soft-polymer windows [34]–[36]. These methods avoid pressing on the brain surface because the sealing materials are designed to fit the curvature of the living brain surface. However, these methods utilize thick sealing materials with a high refractive index, resulting in various optical aberrations. In addition, bleeding during/after the surgery can also occur. Therefore, it is challenging to develop large cranial windows that cover the entire parietal region from the cerebral cortex to the cerebellum because the skull on many blood vessels, including the sagittal sinus and the transverse sinus, should be removed.

Nanosheet

In the field of biomaterials, thin polymer films with a 10–100 nm thickness, also known as nanosheets, have been proposed as novel materials for surgical application [37]–[41] and bioimaging [42]–[46]. Nanosheets have unique properties, including high adhesion strength, flexibility, and transparency. Moreover, nanosheets with a thickness of 200 nm or less have strong physical absorption on the object surface [38], [39].

In a previous study, biocompatible polymer nanosheets were developed to effectively stop bleeding under postoperative conditions without harmful effects [37], [41]. Nanosheets composed of poly (L-lactic acid) (PLLA) have also been developed for glue-free wound dressings [37] and carriers of drug-delivery systems [41], [47], utilizing their biodegradability. Furthermore, various functional nanosheets have been fabricated, such as monolayers, multilayers, and fragments [37], [38], [40] to prevent inflammation and bleeding in living tissue.

As a bioimaging application, fluoropolymer nanosheets with high-water retention properties have been shown to facilitate the long-term observation of fixed mouse brain slices with a larger area [43]. The cell immobilization method was also developed to suspend small molecules, such as liposomes, by using a porous fluoropolymer nanosheet for live cell imaging [42]. It has also been reported that thermosensitive polymer nanosheets enable the visualization of temperature shifts in small living animals [48]. Notably, a novel method was proposed to obtain an extra working distance of the objective lens, in which a fluoropolymer nanosheet was utilized to replace the coverslip [45].

Outline of This Research

In this study, I proposed a novel cranial window that utilizes the PEO-CYTOP nanosheet with a thickness of ~130 nm, in which a single-side surface was hydrophilized by polyethylene oxide (PEO) [46]. These PEO-CYTOP nanosheets firmly adhered to brain surfaces, which suppressed bleeding from superficial veins. Utilizing this nanosheet as a sealing material in the open skull method instead of a glass coverslip, I achieved a larger cranial window covering approximately the entire parietal region. In addition, I

demonstrated two-photon imaging of neural structures with a high spatial resolution as well as the wide-field and long-term time-lapse *in vivo* imaging of Ca^{2+} elevation in the living mouse brain.

Furthermore, I proposed the NIRE method (Nanosheet Improved by light curable REsin method) to make a cranial window that used both the PEO-CYTOP nanosheet and UV curable resin. The UV curable resin laminated the PEO-CYTOP nanosheet on the brain surface. I confirmed that this method suppressed motion artifacts and maintained the transparency of the cranial window for more than 166 days. In addition, the NIRE method successfully enabled the visualization of the neural structure and Ca^{2+} activities in multi-scale from a population of hundreds of neurons down to a single spine in living mouse brains. Finally, the NIRE method successfully demonstrated *in vivo* 3D imaging of neural structures through a large enough cranial window to cover the cerebral cortex to the cerebellum.

Materials and Methods

Fabrication of the PEO-CYTOP Nanosheet

The perfluoro (1-butenyl vinyl ether) polymer, known by the commercial name "CYTOP (CTX-809SP, AGC Inc., Japan)," was dissolved in perfluorotributylamine at a concentration of 30 mg/mL, for spin casting. The substrates were silicon wafers (100) deposited on a 200 nm silicon oxide layer (KST World Corp., Japan) that were freshly cut into an appropriate size before use. PVA (M_w, 22,000; Kanto Chemical Co., Inc., Japan) dissolved in water at 10 mg/mL was dropped onto a substrate and spin-coated at 4000 rpm for 20 s (MS-A100, Mikasa Co., Ltd., Japan), to prepare a sacrificial layer. Subsequently, the CYTOP solution was dropped onto a PVA-coated substrate and spin-coated at 4000 rpm for 60 s. A 10:1 w/w mixture of Sylgard 184 silicone elastomer base and curing agent was dissolved in hexane at a concentration of 1.25 wt% and spin-coated at 4000 rpm for 20 s (Figure S1a). The composite was cured at 80°C for 2 h and then exposed to oxygen plasma at 11 W for 60 s (PDC-32G, Harrick Plasma, Inc., NY, USA). PEO-silane (2-(methoxy(polyethyleneoxy)propyl) trichlorosilane; SIM6492.66; M_w, ~538; Gelest, Inc., PA, USA) was dissolved in toluene at 2 mM for the modification of the hydrophilic surface. The resulting substrate was placed in a Teflon dish filled with silane solution at room temperature (25°C) for 1 h. Finally, the prepared nanosheets were released from the substrate to float on the surface of the water as the sacrificial layer dissolved and were re-supported on a necessary surface for subsequent characterization. It is worth noting that, to adhere the nanosheet to a living mouse brain, they were transferred to the surface of a nonwoven fabric substrate (disposable tea filter bag made from polyethylene and polypropylene, complied with Japanese Food Sanitation Act,

Product Code: H-070 No. 475, Daiso Industries Co., Ltd.), with the hydrophilic side facing outward. All PEO-CYTOP nanosheets in this study were fabricated and provided by Prof. Okamura at Tokai University.

Characterization of the PEO-CYTOP Nanosheet

The thickness of the nanosheets on the silicon wafer was analyzed using a stylus profilometer (DektakXT, Bruker Corp., MA, USA) and estimated as ~130 nm (Figure S2e). The morphology of the nanosheets on the Anodisc membrane (pore size, 0.1 μm; GE Healthcare, IL, USA) was observed via field-emission SEM (S-4800; Hitachi High-Technologies Corp., Japan). The static water contact angle of the nanosheets was measured using a contact angle meter (DMe-211, Kyowa Interface Science Co., Ltd., Japan) at room temperature and relative humidity of 40%. Surface element analysis of the nanosheets was performed before and after surface modification using X-ray photoelectron spectroscopy (PHI Quantera II, Physical Electronics, Inc., MN, USA). The light transmittance of the nanosheets supported on the quartz glass was measured using a UV-Vis-NIR spectrophotometer (V-670, JASCO Corp., Japan) at a wavelength ranging from 300 to 800 nm. The water-retention effect of the nanosheet was evaluated as reported previously [43]. Briefly, an aqueous sodium alginate (Kanto Chemical Co., Inc., Japan) solution at 20 mg/mL was poured into a calcium chloride solution at 2 wt% with a ratio of 1:2 v/v. An alginate hydrogel ball was formed after stirring overnight. Subsequently, the hydrogel was punched into a cylindrical shape with a diameter of 10 mm and a thickness of 3 mm. This was gently placed in the center of a floating nanosheet on the surface of the water with the addition of 100 μL of water. A cover slip with a diameter of 25 mm and a thickness of 0.13–0.16 mm (AS ONE Corp., Japan) was pressed from above

and then enfolded in the margin of the nanosheet using tweezers. The original weights of the wrapped samples at specific time intervals over 24 hours at room temperature and at a relative humidity of 40% were measured as W_0 and W_t, respectively. Samples were then thoroughly dried in an oven at 80°C and weighed as W_d. The water retention ratio was calculated using the following equation: $(W_t - W_d) / (W_0 - W_d) \times 100$ wt%. Moreover, I developed a method to evaluate the improved adhesion capability of the nanosheets after surface modification. The suspension of MNPs with diameters of 10 nm (EMG 707; Ferrotec Corp., CA, USA) was mixed with the sodium alginate solution at a 1:1 v/v ratio. The MNP-loaded hydrogel with a diameter of 3 mm was prepared to model the tissue. To prevent the desiccation of the hydrogel and to simulate the tissue fluid that leaked out of the mouse brain, 1 μL of water was added before the hydrogel was placed on the surface of the nanosheet. A permanent magnet (remanence magnetic flux density, ~480 mT) was gradually placed closer to the sample until the hydrogel could overcome the maximum friction. The distance over which the hydrogel was dragged was called the resistant distance, *d*, and was determined based on a video captured by a digital camera (G7 X Mark II; Canon Inc., Japan). PEO-CYTOP nanosheets were characterized by Professor Okamura at Tokai University.

Animals

Adult, wild-type C57BL/6J mice (over 8 weeks of age, regardless of gender) were used for all experiments. All mice were housed under a 12 h/12 h light/dark cycle. Thy1-EYFP-H (H-line) transgenic mice were used for *in vivo* imaging [49]. H-line mice, which express the enhanced yellow fluorescent protein (EYFP) in a subset of layer 5 pyramidal cells, enabled the capture of fluorescence images that were suitable to visualize neuron structure.

GLT1-G-CaMP7 (G7NG817) transgenic mice expressing the Ca^{2+} indicator G-CaMP7 mainly in astrocytes and a subpopulation of neurons were used to evaluate Ca^{2+} activity [50]. These experiments were conducted in accordance with the recommendations included in the Guidelines for the Care and Use of Laboratory Animals of the Animal Research Committee of Hokkaido University. The procedures were approved by the Institutional Animal Care and Use Committee of the National University Corporation Hokkaido University and the National Institutes of Natural Sciences. These genetic recombination experiments were approved by the Safety Committee on Genetic Recombination Experiments of Hokkaido University and the National Institutes of Natural Sciences. The facility used for the care and management of laboratory animals was approved by the Institutional Animal Care and Use Committee of Hokkaido University and NIPS Recombinant DNA Experiments Safety Committee of National Institute for Physiological Sciences.

Cranial Window Surgery

Mice were anesthetized with 1% isoflurane during surgery. The body temperature of each mouse was maintained using a heating light and/or mat. First, the hair and skin of the mouse were removed to expose the cranial skull. Subsequently, part of the cranial skull was removed with a dental drill to generate a cranial window for *in vivo* imaging of the living mouse brain at high resolution. 20% mannitol (TERUMO Corp., Japan) or GLYCEOL (TAIYO Pharma, Japan) were administered via intraperitoneal injection (15 μL/g), to loosen the dura for 15 minutes before the surgery. A rift was then made in the dura using a tweezer or a 27G needle. Next, a tweezer was carefully inserted under the dura via the rift, to peel it off. Then, 25 μM Sulforhodamine 101 (SR101) was applied

onto the brain surface and incubated for 5 minutes to stain astrocytes. As an adeno-associated virus (AAV) in Figures 21 and 22, AAV-DJ-syn-jGCaMP7f (6.16×10^9 vector genomes/mL, Addgene plasmid # 104488; http://n2t.net/addgene:104488; RRID:Addgene_104488) [51] was used for the expression of Ca^{2+} indicator to achieve *in vivo* two-photon imaging with a high signal-background ratio. After filling a glass pipette with the AAV, the pipette was slowly inserted to a depth of 150 μm from the dura in the brain of a wild-type mouse. Approximately 500 nL of the AAV solution was injected with 10 psi. After the injection, 5% glycerol was administered to mice as drinking water for 2 weeks before the imaging session [52].

After washing dust and blood with phosphate-buffered saline (PBS) or saline, the PEO-CYTOP nanosheet supported by a nonwoven fabric was placed onto the brain surface with the hydrophilic side exposed to the brain surface. The PEO-CYTOP nanosheet was then lightly pushed via the nonwoven fabric using a tweezer, for adherence to the brain surface. After confirmation that the PEO-CYTOP nanosheet had been successfully transferred to the brain surface, the nonwoven fabric was removed. If the nanosheet was misplaced, it was easily removed by dropping PBS or saline onto it and floating the nanosheet from the brain surface. If any bubbles were observed under the PEO-CYTOP nanosheet, they were carefully pushed out using a tweezer or string made from a twisted Kimwipe (NIPPON PAPER CRECIA Co., Ltd., Japan). In large cranial windows, 20% mannitol or GLYCEOL were administered via intraperitoneal injection (15 μL/g), to reduce the intracranial pressure and make the surface as flat as possible. After attaching it, the nanosheet was adjusted to the specified range of the cranial window. The edge of the sheet was glued using cyanoacrylate or blue light curable resin, to prevent soaking of the immersion solution under the PEO-CYTOP nanosheet. When fixing the PEO-CYTOP

nanosheet, the resin remained localized at the edge of the nanosheet because CYTOP exhibits chemical resistance and repellency to both water and oil. However, in the case of observations performed using an air-immersion objective lens, the PEO-CYTOP nanosheet and its edge did not require sealing with the resin. The PEO-CYTOP nanosheet was combined with a glass coverslip to prevent the PEO-CYTOP nanosheet from floating and breaking in long-term observation. The glass coverslip (a circle with a diameter of 4.2 mm, a circle with a diameter of 2.7 mm, and a 5 × 6 mm rectangle; all glass coverslips #1S, approximately 0.17 mm in thickness, Matsunami Glass Ind., Ltd, Japan) was set on top of the PEO-CYTOP nanosheet.

For *in vivo* imaging of an anesthetized mouse, a 35 mm plastic dish was fixed onto the head of the mouse to preserve the immersion solution and suspend the head from the adapter stage, as reported previously [11], [12]. For *in vivo* imaging of awake mice, an aluminum head plate (refer to [53], [54]) was used instead of the plastic dish (Figure 17). The head plate was fixed on the mouse skull with a super-bond (Sun Medical, Japan). A novel stage was designed for an awake mouse to use novel head plates (Figure 17). This stage was 1cm thick and weighed over 1 kg. The stage was made of magnetizing metal and could be set to the base plate mounted with neodymium magnets, which strongly fixed the stage. It also had a hole to hold the tip of the screw so that the screw will not slip when turning.

To examine brain tissue without sealing materials, an annular bank of the light curable resin was made surrounding the cranial hole and filled with saline (Figure 10). A glass coverslip was placed on the top of this bank to avoid direct contact with the brain surface and prevent drying during the 3 days after surgery.

As shown in Figure 3, a crack was introduced in the PEO-CYTOP nanosheet to allow

the flow of water into the gap between the adhesive surface of the nanosheet and the brain surface. By adding a large amount of water, the PEO-CYTOP nanosheet was floated and slightly separated from the brain surface. Thus, the floating nanosheet could be easily removed with tweezers. After removing the PEO-CYTOP nanosheet, another PEO-CYTOP nanosheet could be attached to the surface of the brain.

As shown in Figure 5, a similar cranial window was prepared that was sealed using either a glass coverslip or a PEO-CYTOP nanosheet, in turn. In this process, a cranial window was generated using a PEO-CYTOP nanosheet, (i) two-photon imaging was performed, (ii) the PEO-CYTOP nanosheet was removed, and (iii) the cranial hole was resealed using a glass coverslip and two-photon imaging was performed.

Lamination of UV Curable Resin (NIRE Method)

After sealing a cranial hole with a PEO-CYTOP nanosheet, UV curable resin (NOA83H, Norland Products Inc., USA) was dropped on the PEO-CYTOP nanosheet. The resin was fixed by a manual UV irradiator (JAXMAN, China) or programmable UV irradiator composed of an LED control board (ADULEDB, Bit Trade One, Japan) and UV-LED (OSV1XME3E1S, OptoSupply, Hong Kong) (Figure 14). The programmable irradiator has a wavelength of 365 nm and a radiant power of 200 mW. The optimal irradiation condition to fix the resin with low temperature was 2 seconds of irradiation every 30 seconds for 3 minutes and 10 seconds of irradiation every 30 seconds for 7 minutes with the power at 10 mW. The thickness of the UV curable resin layer was 100–200 μm in this study.

Image Acquisition

All two-photon fluorescence images were obtained through two-photon laser microscopy customized for *in vivo* imaging (A1R-MP+, Nikon). An Olympus XLFLUOR4X/340 4×/0.28 NA air-immersion objective lens for *in vivo* imaging with a broad field of view (FOV) (e.g., Figure 19, 21), Nikon CFI75 LWD 16×/0.80 NA water-immersion objective lens for broad cross-sectional imaging (e.g., Figure 6, 23, 24), and a Nikon Apo LWD 25×/1.10 NA water-immersion objective lens were used for deep *in vivo* imaging (e.g., Figures 4, 5, 7, 9, 12, 15, 19, and 22). When using glass coverslips, the correction collar of the objective lens was adjusted by rotating to 0.17. The refractive index of the immersion solution was changed using glycerin, which has a refractive index of ~1.47. A Ti:Sapphire laser (MaiTai eHP DeepSee, Spectra Physics) was used as an excitation laser light source at a wavelength of 960 nm for EYFP, 920 nm for G-CaMP7, and 950 nm for jGCaMP7f. Image stacks were acquired with Z-steps of either 1 or 5 μm. All fluorescence signals under the 690 nm wavelength were detected by non-descanned detectors equipped with GaAsP PMTs (NDD) at 0.5 or 1 frame per second (fps) for EYFP and 3.8 or 30 fps for G-CaMP7 and jGCaMP7f. The sensitivity of the NDD and the laser power were adjusted according to the experiments. The fluorescence signal was separated with two dichroic mirrors (560-nm dichroic mirror with 500–550 nm for yellow-green beads, EYFP, G-CaMP7, and jGCaMP7f and 593-nm dichroic mirror with 601–657 nm for SR101.

To measure wide-field Ca^{2+} elevations (Figure 9), epi-fluorescence microscopy (AZ100, Nikon) with a Nikon AZ-Plan Fluor 2×/0.20 NA air-immersion objective lens and a mercury lamp (Intensilight C-HGFI, Nikon) was used as the excitation light source.

The fluorescence signals were detected using a CMOS camera (Zyla-5.5, Andor, UK) with a FOV of 16.4 mm × 14.0 mm (2560 × 2160 pixels) at 3.8 fps.

The results of Figures 4–9, 12 were obtained from a mouse under anesthesia. In Figures 7, 16, 18, 19, 21–24, the head-fixation system was used for two-photon imaging in awake mice. The body temperature of the mouse was maintained with a disposable heating pad during imaging.

For fluorescent beads imaging, yellow-green beads (diameter, 200 nm; Invitrogen) were embedded in 1% agarose gel (1:100, v/v). Image stacks were acquired with Z-steps of 0.2 μm. The fluorescent beads images had a pixel size of 50 nm. The full width at half maximum (FWHM) values was calculated by fitting the fluorescence intensity profiles around the central intensity using Gaussian functions in ImageJ. A Nikon Apo LWD 25×/1.10 NA water-immersion objective lens was used in two-photon microscopy (A1R-MP+, Nikon, Japan). For evaluation of the optical property of a cranial window using the NIRE method, a film of UV curable resin was prepared with a thickness of approximately 150 μm.

Immunostaining

Mouse brains were perfusion-fixed with 4.0% paraformaldehyde (PFA) after either 2 weeks (Figure 11) or 4 weeks (Figure 15) after cranial window surgery in the primary visual cortex. After fixing overnight in 4% PFA, coronal slices (50 μm) were cut using a vibratome (7000smz; Campden Instruments Ltd, Leicestershire, UK). The fixed brain slices were then incubated in 10% blocking solution (NACALAI TESQUE, INC., Japan) containing 0.2% Triton X-100 for 30 minutes at room temperature. Following this, slices were incubated with primary antibodies (1:1,000 for anti-glial fibrillary acidic protein

(GFAP) and anti-IBA-1 antibodies, FUJIFILM Wako Pure Chemical Corporation, Japan) overnight (~16 h) at 4°C. After washing with 0.1% Tween 20 in PBS, the slices were incubated with secondary antibodies (1:500; Alexa Fluor 594 donkey anti-mouse IgG and Alexa Fluor 633 donkey anti-rabbit IgG; Thermo Fisher Scientific, Waltham, MA, USA) for 4 h at room temperature. For nuclear staining, 1:2000 Hoechst 33258 stain was used (FUJIFILM Wako Pure Chemical Corporation, Japan). Immunostained slices were examined using confocal microscopy (Leica TCS SP8 STED 3X FALCON, Leica, USA) with an HC PL Fluotar 20×/0.50 NA (Figure 10) and HC PL APO CS2 10x/0.40 NA (Figure 15) dry objective lens.

The areas of activated astrocytes were measured using a NIS element (Ver.4.51, Nikon instrument INC., Japan). The activated area was calculated using Otsu's method [55]. The activated areas in regions of interest (ROIs) were normalized per 100 μm^2.

The Analysis of the Displacement of FOV

The correlation coefficient used in Figures 7 and 18 was calculated by MATLAB (2019b, The MathWorks, Inc., USA). Reference frames are defined by (i) generating a reference frame as the median of all frames, (ii) calculating the correlation coefficient between the reference frame of (i) and each frame, (iii) generating a reference frame again using the median of 10 frames from the top correlation coefficient of (ii), and (iv) calculating the correlation coefficient again between the reference frame of (iii) and each frame.

The Analysis of Ca^{2+} Imaging

The Ca^{2+} imaging data in Figures 8, 9, and 22 were analyzed using imaging software (NIS element, Nikon). The time measurement tool in the software was used for tracing Ca^{2+} activity in the ROIs. The baseline values for the relative fluorescence change (*ΔF/F)* were defined as follows: the mean intensity of the 10 second period from the start of observation in Figure 8, the mean intensity of the 10 second period in Figure 9, and the minimum intensity of each pixel in Figure 22. *ΔF* is the difference of the signal from the baseline.

In Figure 21, the Ca^{2+} activity of neurons was segmented and extracted from time-lapse data using CaImAn [56], based on MATLAB 2021b. This method was initialized with the greedy method to find the components. The number of components was set as 900 from the number of recorded neurons expected in the images. Other parameters for the selection of neurons were set as follows: tau is 12 as half size of neuron, 2 as the minimum SNR threshold, 0.01 as space correlation threshold, and 0.1 as the threshold for the classifier of the convolutional neural network. *ΔF/F* was calculated from the components of neurons as a signal and the background component as a baseline value using the constrained non-negative matrix factorization (CNMF) algorithm in CaImAn.

Results

1. Large-Scale Cranial Windows Using the PEO-CYTOP Nanosheets

The PEO-CYTOP nanosheet is composed of a layer of amorphous perfluoro (1-butenyl vinyl ether) polymer, commercially known as CYTOP, with ~130-nm thickness and a layer of polydimethylsiloxane (PDMS) with a thickness of ~7 nm (Figure 1a). To make the adhesive surface hydrophilic, polyethylene-oxide (PEO) was attached to the surface of the PDMS layer (*see* Materials and Methods, and Appendix). This hydrophilization made it easier for the PEO-CYTOP nanosheet to adhere to a living brain surface.

Next, I sought to determine whether the PEO-CYTOP nanosheet could be used to seal a cranial window covering the whole parietal region of a mouse brain (Figure 1b). First, the skull was removed and the fragments were cleaned as reported [32], [33]. Then, a PEO-CYTOP nanosheet supported by a nonwoven fabric was placed onto the brain surface, with the hydrophilic side of the PEO-CYTOP nanosheet facing the brain surface (Figure 1c, d). In addition, the PEO-CYTOP nanosheet was carefully touched via the nonwoven fabric to transfer the nanosheet to the brain surface (Figure 1e). The fabric was removed after confirming the transfer (Figure 1f). The higher flexibility of the PEO-CYTOP nanosheet enabled the establishment of a larger cranial window that conventional glass coverslips would not be able to seal. The area of the cranial window in Figure 1f was over 50 mm^2.

In addition, the effect of suppressing any bleeding from the veins on the brain surface by the PEO-CYTOP nanosheet served to keep the cranial window clean and devoid of blood clotting (Figure 2). The effect of bleeding suppression was verified when intentionally wounding the right transverse sinus after attaching a nanosheet. The PEO-

CYTOP nanosheet effectively suppressed bleeding from such a superficially injured vein (Figure 3). The blood did not spread over the initial points to the rostral regions beneath the PEO-CYTOP nanosheet. After the resealing of bleeding, re-bleeding did not occur from the injured sinus. Therefore, utilizing the PEO-CYTOP nanosheet allowed for a large-scale cranial window to achieve *in vivo* imaging from the whole parietal region while suppressing bleeding from the brain surface.

2. Characterization of the Optical Properties of the Cranial Window Using the PEO-CYTOP Nanosheet

To evaluate the optical properties of the PEO-CYTOP nanosheets, point spread functions (PSFs) were measured by obtaining fluorescence images of a 200 nm yellow-green beads nanosheet embedded with an agarose gel through the PEO-CYTOP nanosheet and a glass coverslip (Figure 4). The lateral FWHM of PSF through the PEO-CYTOP was 436 ± 1.67 nm (mean ± standard error, 10 beads in each cranial window), and that recorded through the glass coverslip was 437 ± 2.05 nm. There was no significant difference in the lateral FWHM of PSFs between the two materials (Figure 4e). However, the axial FWHM of PSF through the PEO-CYTOP nanosheet was 1.68 ± 0.03 μm and that of the glass coverslip was 1.99 ± 0.02 μm. The axial FWHM of PSF through the PEO-CYTOP nanosheet was significantly narrower (Figure 4h).

Moreover, sequential *in vivo* two-photon imaging of the PFC was performed through an identical cranial window, which was first sealed with the PEO-CYTOP nanosheet followed by resealing with a coverslip after removing the nanosheet (Figure 5). Although the PEO-CYTOP nanosheet did not improve the imaging quality when comparing the images obtained via both cranial windows, the structures of the soma and those of the dendritic branches were not prominently different, even in the deep layers. Thus, it was confirmed that the PEO-CYTOP nanosheet could be used for *in vivo* two-photon imaging as a sealing material of the cranial window that did not deteriorate the neural structure in deep and wide-field imaging.

3. *In Vivo* Two-Photon Large-Scale Imaging of Neural Morphology with the PEO-CYTOP Nanosheet

To confirm that the cranial windows afforded by the PEO-CYTOP nanosheet were compatible with *in vivo* mouse brain imaging, *in vivo* two-photon imaging was conducted in Thy1-EYFP-H mice [49] (Figure 6a–f). Several series of fluorescent images of the living mouse brain were collected crossing the superior sagittal sinus both vertically (over 3 mm in length), and parallel (over 6 mm in length), as shown in Figures 6b and 6c, respectively. Under these conditions, fluorescent images were obtained at a sub-cellular resolution (Figure 6d–f). The curvature of the brain shown in Figure 6b and 6c indicated that the brain surface was not distorted. The axons and the dendrites were visualized in cross-sectional *xy*-images with EYFP fluorescence (Figure 6d). The pyramidal neurons were visualized at a deeper layer, up to a depth of 700 μm, corresponding to layer 6 of the primary visual cortex (Figure 6e and 6f). Thus, it was confirmed that the PEO-CYTOP nanosheet could be used for *in vivo* two-photon imaging as a sealing material of the cranial window, and that it did not deteriorate the neural structure in deep and wide-field imaging.

4. Evaluation of Motion Artifacts in Awake and Anesthetized Mice Through Cranial Windows Using Glass Coverslip and PEO-CYTOP Nanosheet

To assess the displacement of the FOV by motion artifacts under both anesthetized and awake conditions, the movements of astrocytes stained with SR101 were monitored, through three types of cranial windows (Figure 7). These types included: (i) a cranial window with a diameter of 4.2 mm sealed with a glass coverslip (Figure 7b), (ii) sealed with a PEO-CYTOP nanosheet (Figure 7f), and (iii) a cranial window with a diameter of >8 mm sealed with a PEO-CYTOP nanosheet (Figure 7j). After acquiring time-lapse imaging through each cranial window, the correlation coefficient was calculated between the reference frame and each frame to compare the displacement of FOV (*see* Material and Methods). As depicted in Figures 7c and 7d, the glass coverslip suppressed the displacement of the FOV because the coverslip pressed the brain tissue tightly. In the case of the PEO-CYTOP nanosheet (Figures 7g, h, k, l), the displacement resulting from respiratory and/or fatal movements were not suppressed completely, however, the natural curvature of the brain surface was maintained.

5. Calcium Imaging in a Broad FOV with the PEO-CYTOP Nanosheet

To evaluate the effects of PEO-CYTOP nanosheets on neural activities, *in vivo* Ca^{2+} imaging was conducted in G7NG817 transgenic mice, expressing the Ca^{2+} indicator G-CaMP7 in astrocytes and a subpopulation of neurons [50]. As shown in Figure 8a, Ca^{2+} elevations were observed by epi-fluorescence microscopy through a large cranial window utilizing a PEO-CYTOP nanosheet. Significant transient fluorescent Ca^{2+} elevations were observed in multiple regions during tail pinch stimulation (Figures 8b and 8c). Thus, the PEO-CYTOP nanosheet enabled *in vivo* imaging of Ca^{2+} elevations in a large FOV.

6. Chronic Window Combining the PEO-CYTOP Nanosheet with Glass Coverslip for *In Vivo* Two-Photon Imaging

To confirm that the PEO-CYTOP nanosheet is not harmful to the neural activities in a living mouse during longitudinal observations, *in vivo* two-photon Ca^{2+} imaging was performed in an identical G7NG817 mouse for 4–9 weeks after surgery. A glass coverslip was placed on the cranial window sealed with a PEO-CYTOP nanosheet to protect against mouse behaviors, including scratching (Figures 9a and 9b). The results showed that the brain tissue without any protectors resulted in edema and bleeding from the brain tissue (Figure 10). At 4–9 weeks post-surgery, the transparency of the cranial window was maintained, with a success rate of 87.5% (14 out of 16 mice). Cells were also visualized at a depth of ~150 μm from G-CaMP7 signals, for long-term imaging (Figures 9c, d, e). Astrocytes were successfully observed up to a depth of 230 ± 59 μm (mean ± standard error, n = 4 animals) at 4 weeks post-surgery. The fluorescence intensity changes, $\Delta F/F$, resulting from Ca^{2+} elevations are presented in Figures 9f and 9g. Neurons and astrocytes were classified according to structural characteristics and the timescale of Ca^{2+} activity as described previously [57]. The G-CaMP7 signals of both neurons and astrocytes were observed even at 9 weeks post-surgery.

To assess the suppression of inflammation by the PEO-CYTOP nanosheet, activated astrocytes were immunostained for the GFAP 2 weeks after surgery (Figure 11). To evaluate the degree of inflammation, the size of the areas occupied by activated astrocytes was assessed using Otsu's method [55]. The activated areas in ROIs per unit area (100 μm^2) were measured. Compared with glass coverslips, the PEO-CYTOP nanosheet suppressed the activated area of astrocytes significantly (0.014% ± 0.001% to 0.006% ±

0.001%, mean ± standard error; 6 ROIs from two mice in each condition) (Figure 11). Therefore, the PEO-CYTOP nanosheet can be applied for long-term imaging while maintaining healthy conditions for brain tissue.

Next, I evaluated whether the PEO-CYTOP nanosheet could be used as a substitute for the dura. Here a PEO-CYTOP nanosheet was attached after the removal of the dura (Figure 12a). A glass coverslip was placed onto the nanosheet (Figure 12b) to protect the cranial window for long-term imaging as shown in Figure 9a. In this case, the removal of the dura frequently triggered bleeding and injuries because of the dissection of blood vessels connecting the dura with the brain tissues. However, the PEO-CYTOP nanosheet could suppress bleeding and injuries resulting from mechanical stress to the brain surface in the absence of the dura. In this cranial window, optical transparency was maintained for 14 weeks post-surgery. Dura regrowth and blood coagulation did not occur (Figure 12b). Ultimately, long-term two-photon imaging in Thy1-EYFP-H mice in which the dura was replaced with a PEO-CYTOP nanosheet (Figure 12c, d) was successful. The same neuron and axon in the same period could be observed.

7. The NIRE Method to Create the Cranial Window Combined with the PEO-CYTOP Nanosheet and Light Curable Resin

The remaining issues of a cranial window utilizing the PEO-CYTOP nanosheet were the motion artifacts and the difficulty of long-term imaging without the use of a glass coverslip (*See* Results 4 and 6). Thus, the NIRE method was devised to make a large cranial window that combines the PEO-CYTOP nanosheet with UV curable resin (Figure 13a). This method aimed to suppress motion artifacts in awake mice and to enable long-term imaging of the living mouse brain with a broad FOV.

To demonstrate this method, UV curable resin produced for optic parts as a sealing material was used to offer high transparency and fit to the shape of the brain surface. I examined whether UV curable resin could be fixed on the PEO-CYTOP nanosheet. First, the brain surface of the mouse was exposed (Figure 13b) and sealed with the PEO-CYTOP nanosheet (Figure 13c) as in Figure 1f. Next, the surface of the PEO-CYTOP nanosheet was coated with UV curable resin and irradiated with a UV irradiator (Figure 13d). Through these steps, a large cranial window covered with a PEO-CYTOP nanosheet and UV curable resin was achieved without pressing the brain surface strongly.

8. Evaluation of Heat Production and Inflammation in the NIRE Method

With the application of UV curable resin as a sealing material, one concern was that heat production could cause brain damage during the curing of the resin. To solve this problem, a time and power programmable UV irradiator composed of a UV-LED and an LED control board was made to control the timing of irradiation and UV power (Figure 14a).

The protocol was optimized to achieve full curing without high heat production (Figures 14b and 14c). To determine changes in heat production, a thermometer electrode was inserted into UV curable resin on a plastic dish to measure the temperature during UV irradiation. In continuous UV irradiation, the temperature inside the resin immediately reached over 40 ℃ (within the first 30 seconds of irradiation of the 10-minute duration in Figure 14b). By contrast, intermittent UV irradiation did not reach an elevated temperature because the temperature repeatedly rose and fell following the irradiation (2 seconds irradiation every 30 seconds for 3 minutes and 10 seconds irradiation every 30 seconds for 7 minutes in Figure 14c). Thus, intermittent irradiation was determined as the optimal condition as indicated in Figure 14c.

To evaluate the heat-induced damage and inflammation by the NIRE method, activated astrocytes and microglia were immunostained by GFAP and Iba1 antibodies in three types of cranial windows. These included: (i) a cranial window using UV curable resin only (without a PEO-CYTOP nanosheet) in the optimal irradiating conditions (Figure 15a), (ii) a cranial window using the NIRE method in optimal irradiating conditions (Figure 15b) and (iii) a cranial window using the NIRE method with high power irradiating conditions

(Figure 15c). In the optimal irradiating conditions, the activated area of astrocytes and microglia was suppressed in the cranial window using the NIRE method compared with UV curable resin only (Figure 15a, b). By contrast, the astrocytes in the cranial window with high power irradiation were most activated in all cranial windows (Figure 15c). Therefore, the intermittent irradiating condition shown above was most optimal to fix the resin without heat damage to the brain tissue. In addition, the PEO-CYTOP nanosheet suppressed inflammation induced by UV curable resin.

9. Evaluation of the Optical Properties of the Cranial Window Using the NIRE Method

To verify the optical properties of the cranial window using the NIRE method, PSFs were measured by obtaining fluorescent images of a 200 nm yellow-green beads nanosheet embedded with an agarose gel at depths of 200, 500, and 1000 μm (Figure 16). The lateral FWHM of PSF at each depth was 559 ± 4.84 nm at 200 μm, 564 ± 5.12 nm at 500 μm, and 615 ± 7.81 nm at 1000 μm (mean ± standard error, 10 beads in each depth). There was no significant difference in the lateral FWHM of PSFs between the 200 and 500 μm depths (Figure 16b, e). The lateral FWHM of PSFs of the 1000 μm depth was significantly wider compared to other depths. On the other hand, the axial FWHM of PSF at each depth was 4.02 ± 0.08 μm at 200 μm, 4.67 ± 0.05 μm at 500 μm, and 6.48 ± 0.09 μm at 1000 μm. When comparing the three depths, the axial FWHM of PSF was significantly wider as the depth increased.

Therefore, the spatial resolution was sufficient to observe neural structures and activities. However, the spatial resolution in deep regions was significantly deteriorated likely due to a high refractive index, scattering, and a non-uniform surface.

10. Evaluation of Motion Artifacts in Awake Mice Through the Cranial Window with the NIRE Method

As shown in Figure 7, motion artifacts disable the visualization of neural activities at a high temporal resolution. To suppress motion artifacts by body movements of an awake mouse, a metal head plate and stage to fix the plate were adapted (Figure 17, *see* Materials and Methods). Using this setup, the displacement of the FOV during imaging sessions against the motion artifact under anesthetized and awake conditions in the NIRE method were assessed (Figure 18). Astrocytes stained with SR101 were observed as in Figure 7. The correlation coefficient between the reference frame and each frame was evaluated (*see* Material and Methods). As depicted in Figure 18a–d, the PEO-CYTOP nanosheet did not suppress the displacement of the FOV because it could not press the brain surface. In contrast, the UV curable resin could suppress the displacement significantly. Thus, the UV curable resin was effective to fix on the curved surface of the living brain and suppressed the motion artifact in *in vivo* imaging of the mouse brain.

11. *In Vivo* Multi-Scale Imaging of Neural Morphology Using the NIRE Method

To demonstrate long-term imaging using the NIRE method, *in vivo* two-photon imaging in Thy1-EYFP-H mice was conducted (Figure 19). The transparency of the cranial window was maintained for 20 days post-surgery (Figure 19a). Bleeding occurred under the dura, as shown in the right photos of Figure 19a. However, the blood was cleaned up 10 days after surgery.

Through the large cranial window, fluorescent images with a broader FOV were obtained using a 4× magnification objective lens (~7.8 mm × ~6.0 mm) (Figure 19b). To examine the microstructure of neurons, the axons and dendrites in cross-sectional *xy*-images at a depth of 100 μm using a 25× magnification objective lens were visualized (Figure 19c). In the same plane as Figure 19c, the dendritic spines were observed at sub-cellular resolution (Figure 19d). Therefore, *in vivo* multi-scale imaging of neural structures ranging from the whole parietal cortex to microstructures like dendric spines is achievable with the NIRE method. This method allows for the observation of morphological changes from synapses in a small region to dendrites and axons in multiple regions of the cerebral cortex.

12. *In Vivo* Multi-Scale Ca^{2+} Imaging in Awake Mice Using the NIRE Method

To assess the capacity to measure neural activities, an AAV-encoding Ca^{2+} indicator (AAV-DJ-syn-jGCaMP7f) was injected at a depth of 150 μm in the somatosensory cortex in wild-type mice. The cranial window using the NIRE method was made in each mouse immediately after injection (Figure 20a). The transparency of the cranial window was maintained for over 166 days, at a success rate of 75% (3 out of 4 mice) (Figure 20b). The proliferation of blood vessels did occur but the cranial window was not clouded, and thereby, did not interfere with *in vivo* two-photon imaging.

In vivo large-scale Ca^{2+} imaging in the primary somatosensory cortex with a broader FOV was performed through the cranial window as shown in Figure 20. Figure 21a shows the maximum intensity projection rendered from time-lapse imaging data using a 4× magnification objective lens. Wide-field *xy*-images (~2.1 mm × ~2.1 mm) at 3.8 fps were recorded. Overall, 802 neurons were identified in a 5-minute recording (Figure 21b). The fluorescence intensity changes of each neuron were calculated by the CNMF algorithm of CaImAn (*see* Materials and Methods).

To verify the spatial resolution through the cranial window using the NIRE method, spontaneous Ca^{2+} activity from finer structures including dendrites and dendric spines could be detected in the same mouse of Figures 20 and 21 at a depth of 150 μm, using a 25× magnification objective lens (Figure 22a). The fluorescence intensity change from the time-lapse images (Figure 22b) was calculated and the activity from the ROIs on the dendritic spines (Figure 22c) was tracked. The peaks of $\Delta F/F$ in each region ranged from 85 to 245%. Clearly, the cranial window using the NIRE method allowed *in vivo* multi-

scale Ca^{2+} imaging in the cerebral cortex of an awake mouse more than 166 days after the surgery.

13. Extended Large-Scale Cranial Window Using the NIRE Method

To demonstrate the application of the NIRE method in a larger cranial window with high curvature, cranial windows covering the cerebellum and midbrain (Figure 23a) were created. The transparency of the cranial window was monitored for 10 days post-surgery. Bleeding under the dura occurred, as shown in the right photos of Figure 23a. However, the blood was cleaned up 10 days after surgery. In addition, *in vivo* two-photon imaging was performed in Thy1-EYFP-H mice (Figure 23a). Three-dimensional stacks of neuron structures with a broader FOV (~ 3.0 mm × ~ 0.8 mm) were obtained using a 16× magnification objective lens at sub-cellular resolution (Figures 23b and 23c). As shown in the side view of the stacks (Figure 23b), the curved surface of the mouse brain was maintained. Parallel fibers and granular cells located in the cerebellum were visualized at a depth of 200 μm. Neuron structures such as dendrites and cell bodies in the midbrain at a depth of 400 μm were also observed.

Moreover, a much larger cranial window covering the cerebral cortex to the cerebellum was made in Thy1-EYFP-H mice (Figure 24a). *In vivo* two-photon imaging was performed and three-dimensional stacks of neuron structures with a broader FOV (~ 2.4 mm × ~ 1.7 mm) were created using a 16× magnification objective lens at sub-cellular resolution (Figures 24b-d). The curved surface of the mouse brain was maintained as shown in the side view of the stacks (Figures 24b and 24c). Structures of each region were visualized, such as axons and dendrites in both the cerebral cortex and midbrain, and granular cells in the cerebellum (Figure 24d).

In conclusion, this novel, large cranial window enables the visualization of neural structures from the cerebral cortex to the cerebellum using the NIRE method.

Discussion

In this study, a PEO-CYTOP nanosheet as a sealing material for a cranial window in the open skull method successfully enabled the visualization of neural morphology and Ca^{2+} elevations with a broader FOV in the mouse brain (Figures 1–12). Additionally, the NIRE method successfully enabled a large cranial window for the reduction of motion artifacts and long-term imaging of the living mouse brain (Figures 13–18). Through the cranial window, *in vivo* multi-scale, long-term imaging of neural structure and function was achievable in the living mouse brain (Figures 19–22). Finally, the application area of the cranial window was extended to an extra-large cranial window covering the cerebral cortex to the cerebellum (Figures 23 and 24).

Suppression of Bleeding by the PEO-CYTOP Nanosheet

The PEO-CYTOP nanosheet sealed the injured blood vessels tightly and suppressed bleeding from the brain surface because of the high adhesive strength resulting from physical adsorption, such as van der Waals interactions [37], [41]. Previously, several biocompatible nanosheets, including a poly(L-lactic acid) (PLLA) nanosheet, were applied for the suppression of bleeding from various organs, including the stomach, liver, and inferior vena cava [37], [38], [41]. In contrast, CYTOP nanosheets exhibited the potential as a material for living-tissue imaging because of their excellent water retention and surface adhesion. However, CYTOP nanosheets could not be attached firmly to the brain surface because of the high hydrophobicity of CYTOP. To overcome this, the adhesive surface of the CYTOP nanosheet was modified by coating it with PDMS and attaching PEO [46]. This hydrophilization of the nanosheet surface enhanced the adhesion

strength to wet specimens, resulting in the suppression of bleeding from the brain surface (Figures 2 and 3). Thus, the PEO-CYTOP nanosheet could apply to effectively prevent bleeding from the wet surface of living tissues other than the brain.

The Optical Properties in the PEO-CYTOP Nanosheet and the NIRE Method

The optical disturbance caused by the PEO-CYTOP nanosheet was almost negligible compared with the conventional glass coverslip because the thickness of the PEO-CYTOP nanosheet was ~10^{-3} smaller than that of the glass coverslip [32], [33] (PEO-CYTOP nanosheet, ~130 nm; conventional glass coverslip, ~170 μm), and even smaller than the wavelength of visible light. In a method described previously based on a similar concept [34], a PDMS film with a thickness of 300 μm was applied. In contrast, the thickness of the PEO-CYTOP nanosheet used in this study was approximately 100 nm, which enables strong adhesion and suppression of inflammation and bleeding from the brain tissue. Moreover, the refractive index of CYTOP is ~1.34, which is most like that of water (~1.33) but lower than that of glass (~1.54) and PDMS (~1.41). Furthermore, the PEO-CYTOP nanosheet had approximately 100% transmittance [46]. The water permeability of CYTOP was smaller than that of PDMS per unit of thickness, which resulted in the excellent water-retention effect of the PEO-CYTOP nanosheet, even at nano-order thickness. Therefore, the PEO-CYTOP nanosheet can be used as a sealing material for *in vivo* brain imaging with minimal effects from incident lights.

However, an optical disturbance was caused due to the application of UV curable resin, especially in a deep region compared with the PEO-CYTOP nanosheet and the

conventional glass coverslip (Figures 4 and 16). The spatial resolution via the UV curable resin was deteriorated probably because of scattering, its high refractive index (~ 1.56) that caused spherical aberration, and its non-uniform surface causing coma and astigmatism. It will be necessary to use adaptive optics techniques [58]–[62], and/or UV curable resins with low refractive indices to achieve *in vivo* imaging of mouse brains at high resolution, compensating for the refractive index mismatch.

In general, a cranial window with a broad FOV is prone to generate optical aberrations, such as coma or astigmatism, resulting from the curvature of the living brain surface. In conventional cranial windows [33], [63], a planar glass coverslip is suitable for reducing these aberrations. However, a large cranial window cannot be sealed with a planar glass coverslip, because the brain surface is pressed resulting in hindered physiological conditions such as blood flow and the deterioration of cerebrospinal fluid. Thus, cranial windows with a broad FOV like that presented here should be combined with adaptive optical techniques [58]–[62] to achieve *in vivo* imaging at a higher resolution.

The Thermal Properties of the Cranial Window Using a PEO-CYTOP Nanosheet and the NIRE Method

Recent studies report that brain temperatures during *in vivo* imaging affect blood flow and oxygen partial pressures in the brain [64]. Therefore, the thermal properties between the PEO-CYTOP nanosheet and a glass coverslip were compared. Differences lie in the thickness between ~130 nm (PEO-CYTOP) and ~170 μm (glass coverslip) and the thermal conductivity between ~0.12 W/mK (PEO-CYTOP) and ~1.1 W/mK (glass coverslip). Considering these properties, a cranial window with a PEO-CYTOP nanosheet

is ~80 times more heat-transferable than a glass coverslip. Thus, the PEO-CYTOP nanosheet can control the brain temperature effectively to maintain suitable conditions for the brain tissue by changing the temperature of immersion liquid during an imaging session.

On the other hand, the heat production during the curing of the UV curable resin did not affect the brain tissue, which was verified in Figures 14 and 15. The long-term preservation of the transparency of the cranial window using the NIRE method also demonstrated that the heat production did not cause brain damage.

Large Cranial Window Using a PEO-CYTOP Nanosheet

Researchers have proposed several novel techniques to make a cranial window with a broad FOV [34]–[36] to observe the living brain. In this study, a unique sealing material was utilized to enlarge the size of the cranial window. This was previously limited because glass coverslips cannot follow the curvature of the brain surface. Specifically, a larger cranial window over 8 mm in diameter was achieved, compared to the typical size of 2–5 mm in diameter [32], [33].

Recently, a skull clearing method using novel reagents has been proposed to make a large cranial window [30], [31]. The procedure was less invasive and did not require complicated surgical processes. However, it was difficult to apply these methods for observation of the cerebellum and midbrain because the skull covering these regions was very thick and connected with many blood vessels. In addition, the skull also covered the brain surface with the high curvature in the cerebellum and the midbrain, which makes it difficult to clear the skull and achieve *in vivo* imaging with high resolution. Thus, the cranial window using the NIRE method is useful for *in vivo* imaging in the cerebellum

and the midbrain at high resolution (Figure 23, 24).

Motion Artifacts in Cranial Windows Using a PEO-CYTOP Nanosheet and the NIRE Method

As shown in Figure 7, glass coverslips suppressed the motion artifacts by pressing the brain surface tightly. However, the glass coverslips were not suitable for preserving the physiological conditions because the brain tissue was forcefully flattened. Conversely, the PEO-CYTOP nanosheet preserved the physiological conditions, thus avoiding mechanical stress inside the brain and causing no disturbance to the flow of cerebrospinal fluid and blood. To satisfy both the maintenance of physiological conditions and the suppression of motion artifacts, the PEO-CYTOP nanosheet was laminated with UV curable resin (Figure 18). As an alternative way to suppress the displacement of FOV, real-time movement correction systems [65], [66] can also accomplish the stabilization of the FOV against motion artifacts in a cranial window using only the PEO-CYTOP nanosheet.

Long-term Imaging Using a PEO-CYTOP Nanosheet and the NIRE Method

The results presented in Figures 9, 12, and 19–23 demonstrate that the PEO-CYTOP nanosheet can be applied for long-term imaging of the living mouse brain without causing severe inflammation or bleeding. The PEO-CYTOP nanosheet protected the brain surface from contact with foreign substances, including UV curable resin, which caused inflammation, such as fine dust, mouse hairs, and glue to fix the sealing materials in the

operation (Figure 15). Moreover, the chemical properties of CYTOP prevent the decomposition of the nanosheet during long-term imaging because CYTOP is a chemically inert and non-biodegradable fluoropolymer [67]. In addition, PEO is highly biocompatible. It is used as a coating material for medical equipment because hydrated water molecules on the PEO surface might suppress inflammatory reactions [68]. Therefore, the PEO surface of the nanosheet probably inhibited the inflammation compared with a glass surface and UV curable resin. This result was also supported by previous studies that indicated that biocompatible nanosheets inhibited inflammation and bleeding in living tissues [40]. Notably, no unusual behaviors or symptoms of infection were observed in the mice for over a year post-surgery. *In vivo* imaging with a broad FOV at a sub-cellular resolution was achieved in the same mouse over approximately a half year through the cranial window using the NIRE method (Figure 20). Therefore, this method contributes to the large-scale search and analysis for the disease-related regions in disease model animals.

Even in the case of the PEO-CYTOP nanosheet, regrowth of the dura and/or proliferation of blood vessels in the dura, connective tissues, and immune cells on the brain surface sometimes occurred over a week after surgery (Figures 9, 12, and 23) [32], [69], [70]. The regrowth of the dura frequently occurred when the brain surface was not sufficiently sealed with a glass coverslip [32], [69]. In this study, the regrowth and proliferation were remarkably suppressed by replacing the dura with the PEO-CYTOP nanosheet. Previously, researchers have reported several artificial dura substitutes composed of biocompatible polymers, including PDMS, that can inhibit inflammation and maintain healthy conditions in the mammalian brain after removal of the dura [34], [71], [72]. Especially in rats and marmosets, the removal of the dura is required for *in*

vivo two-photon imaging because it is much thicker and opaquer than that of mice [73], [74]. Thus, the PEO-CYTOP nanosheet may be useful for *in vivo* two-photon imaging as an artificial dura substitute in various animals.

Other Applications of the PEO-CYTOP Nanosheet

In a previous study, a porous nanosheet allowed drugs to permeate into the sealed object [42]. It would also be possible to administer drugs to nanosheet-sealed objects using solid inserts, including a microcapillary or a needle. In this study, an AAV injection could be given in the mouse, penetrating the PEO-CYTOP nanosheet (data not shown). Moreover, the PEO-CYTOP nanosheet would allow the simultaneous recording of *in vivo* fluorescent images and electrophysiological data, because of its tolerance to the insertion of solid electrodes.

In addition, optical measurement of neural activity in freely moving animals has been conducted to reveal the neurological bases for social interaction [18], [75]–[79]. Large-scale imaging of neural activity in freely moving mice was generally performed through the skull, which reduced the signal-to-noise ratio and made it difficult to detect signals from deep regions. On the contrary, the cranial window using the NIRE method is expected to facilitate both a higher signal-to-noise ratio and observations in deep brain regions of freely moving mice.

Conclusion and Future Perspectives

In conclusion, the PEO-CYTOP nanosheet enabled the suppression of bleeding from a brain surface and *in vivo* deep and wide-field imaging of the living mouse brain.

Furthermore, the NIRE method allowed *in vivo* multi-scale imaging of neuronal structures and Ca^{2+} activity ranging from a spine of a single neuron to several hundred neurons in the same mouse brain. The NIRE method also facilitated a super large cranial window covering the cerebral cortex to the cerebellum. This novel technique may promote the understanding of the anatomical and functional connectivity between multiple cortical regions in living animal brains by improving the surgical procedure and expanding the optically observable regions.

Future studies will aim to combine the cranial window in this study with novel large-scale imaging systems reported in recent years [14]–[25]. For example, the system with the broadest FOV (14.6 mm × 10.1 mm [17]) was larger than the cranial window in this study (~ 8 mm in diameter). Thus, such a large-scale imaging system can effectively use the large cranial window, which could contribute to the understanding of mechanisms underlying brain functions composed of synchronous activities in multiple brain regions.

Acknowledgments

I am very grateful to Prof. Tomomi Nemoto for many valuable supports and helpful advice about the research contents and the writing of this article as the supervisor. I am also thankful to Prof. Yosuke Okamura, Dr. Hong Zhang and Mr. Kenji Yarinome at Tokai University, for giving me many nanosheets and technical advice about nanosheets. I also thank Dr. Ryosuke Kawakami at Ehime University, for his technical advice about two-photon imaging and open skull surgery. I thank Prof. Junichi Nabekura, Dr. Masakazu Agetsuma, Mrs. Tomoko Kobayashi at the Division of Homeostatic Development, National Institute for Physiological Sciences, National Institutes of Natural Sciences, for the technical support and advice regarding the experiments using awake mice. I also thank Dr. Kohei Otomo at Graduate School of Medicine, Juntendo University for very helpful advice, especially in optics.

I would like to thank Dr. Makoto Higuchi, Dr. Hiroyuki Takuwa, and Ms. Manami Takahashi at the Department of Functional Brain Imaging Research, National Institute of Radiological Sciences, for technical advice regarding the long-term experiments. In addition, some experiments were conducted with the technical and equipment cooperation of the Nikon Imaging Center, Hokkaido University. I also thank Dr. Hajime Hirase (RIKEN CBS) for giving us G7NG817. I also thank the Genetically-Encoded Neuronal Indicator and Effector Project and the Janelia Farm Research Campus of the Howard Hughes Medical Institute for sharing jGCaMP7f constructs.

I would gratefully thank to the member of my thesis committee Prof. Yumiko Yoshimura of Division of Visual Information Processing, National Institute for Physiological Sciences; Prof. Keiichi Kitajo of Division of Neural Dynamics, National

Institute for Physiological Sciences; Prof. Kohei Soga of Department of Materials Science and Technology, Tokyo University of Science.

I sincerely thank Dr. Ryosuke Enoki, Dr. Hirokazu Ishii, Dr. Motosuke Tsutsumi and Dr. Kazushi Yamaguchi at Biophotonics Research Group, Exploratory Research Center on Life and Living Systems (ExCELLS), National Institutes of Natural Sciences for their valuable supports and helpful advice. I really thank all members of my laboratory, Dr. Lee Ming-Liang, Mrs. Chang Ching-pu, Mr. Mitsutoshi Ataka, Mr. Sota Hiro, Mr. Kaito Nakata, Mrs. Kana Tsuchiya, Ms. Yuki Watakabe, Mrs. Chiemi Hyodoh, Mrs. Maki Watanabe, Mrs. Miwa Kawachi and all alumni and alumnae. I deeply appreciate all of those who supported my research and daily life.

References

Figure 1-12 and S1, S2 were referenced and partially modified from [46].

[1] O. Sporns, G. Tononi, and R. Kötter, “The human connectome: A structural description of the human brain,” *PLoS Computational Biology*. 2005. doi: 10.1371/journal.pcbi.0010042.

[2] H. Okano *et al.*, “Brain/MINDS: A Japanese National Brain Project for Marmoset Neuroscience,” *Neuron*, vol. 92, no. 3, pp. 582–590, Nov. 2016, doi: 10.1016/J.NEURON.2016.10.018.

[3] T. Ebina *et al.*, “Two-photon imaging of neuronal activity in motor cortex of marmosets during upper-limb movement tasks,” *Nature Communications*, vol. 9, no. 1, p. 1879, Dec. 2018, doi: 10.1038/s41467-018-04286-6.

[4] P. Theer, M. T. Hasan, and W. Denk, “Two-photon imaging to a depth of 1000 μm in living brains by use of a Ti:Al_2O_3 regenerative amplifier,” *Optics Letters*, vol. 28, no. 12, p. 1022, 2003, doi: 10.1364/OL.28.001022.

[5] M. Kondo, K. Kobayashi, M. Ohkura, J. Nakai, and M. Matsuzaki, “Two-photon calcium imaging of the medial prefrontal cortex and hippocampus without cortical invasion,” *eLife*, vol. 6, Sep. 2017, doi: 10.7554/eLife.26839.

[6] O. Sadakane *et al.*, “In Vivo Two-Photon Imaging of Dendritic Spines in Marmoset Neocortex,” *eNeuro*, vol. 2, no. 4, p. ENEURO.0019-15.2015, Sep. 2015, doi: 10.1523/ENEURO.0019-15.2015.

[7] O. Sadakane *et al.*, “Long-Term Two-Photon Calcium Imaging of Neuronal Populations with Subcellular Resolution in Adult Non-human Primates,” *Cell Reports*, vol. 13, no. 9, pp. 1989–1999, 2015, doi: 10.1016/j.celrep.2015.10.050.

[8] F. Helmchen and W. Denk, “Deep tissue two-photon microscopy,” *Nature Methods*,

vol. 2, no. 12, pp. 932–940, Dec. 2005, doi: 10.1038/nmeth818.

[9] W. Denk, J. Strickler, and W. Webb, “Two-photon laser scanning fluorescence microscopy,” *Science*, vol. 248, no. 4951, pp. 73–76, Apr. 1990, doi: 10.1126/science.2321027.

[10] C. Stosiek, O. Garaschuk, K. Holthoff, and A. Konnerth, “In vivo two-photon calcium imaging of neuronal networks,” *Proceedings of the National Academy of Sciences*, vol. 100, no. 12, pp. 7319–7324, Jun. 2003, doi: 10.1073/pnas.1232232100.

[11] R. Kawakami *et al.*, “Visualizing hippocampal neurons with in vivo two-photon microscopy using a 1030 nm picosecond pulse laser,” *Scientific Reports*, vol. 3, pp. 1–7, 2013, doi: 10.1038/srep01014.

[12] R. Kawakami *et al.*, “In vivo two-photon imaging of mouse hippocampal neurons in dentate gyrus using a light source based on a high-peak power gain-switched laser diode,” *Biomedical Optics Express*, vol. 6, no. 3, p. 891, 2015, doi: 10.1364/boe.6.000891.

[13] B. Li, C. Wu, M. Wang, K. Charan, and C. Xu, “An adaptive excitation source for high-speed multiphoton microscopy,” *Nature Methods*, vol. 17, no. 2, pp. 163–166, 2020, doi: 10.1038/s41592-019-0663-9.

[14] C. Yu‡, J. N. Stirman‡, Y. Yu, R. Hira, and S. L. Smith, “Diesel2p mesoscope with dual independent scan engines for flexible capture of dynamics in distributed neural circuitry,” vol. 8, pp. 1–22, 2020, doi: 10.1101/2020.09.20.305508.

[15] J. N. Stirman, I. T. Smith, M. W. Kudenov, and S. L. Smith, “Wide field-of-view, multi-region, two-photon imaging of neuronal activity in the mammalian brain,” *Nature Biotechnology*, vol. 34, no. 8, pp. 857–862, Aug. 2016, doi:

10.1038/nbt.3594.

[16] K. Ota *et al.*, “Fast, cell-resolution, contiguous-wide two-photon imaging to reveal functional network architectures across multi-modal cortical areas,” *Neuron*, vol. 109, no. 11, pp. 1810-1824.e9, 2021, doi: 10.1016/j.neuron.2021.03.032.

[17] T. Ichimura *et al.*, “Exploring rare cellular activity in more than one million cells by a transscale scope,” *Scientific Reports*, vol. 11, no. 1, pp. 1–16, 2021, doi: 10.1038/s41598-021-95930-7.

[18] K. K. Ghosh *et al.*, “Miniaturized integration of a fluorescence microscope,” *Nature Methods*, vol. 8, no. 10, pp. 871–878, Oct. 2011, doi: 10.1038/nmeth.1694.

[19] D. R. Sparta, A. M. Stamatakis, J. L. Phillips, N. Hovelsø, R. van Zessen, and G. D. Stuber, “Construction of implantable optical fibers for long-term optogenetic manipulation of neural circuits,” *Nature Protocols*, vol. 7, no. 1, pp. 12–23, Jan. 2012, doi: 10.1038/nprot.2011.413.

[20] E. Yoshida *et al.*, “In vivo wide-field calcium imaging of mouse thalamocortical synapses with an 8 K ultra-high-definition camera,” *Scientific Reports*, vol. 8, no. 1, p. 8324, Dec. 2018, doi: 10.1038/s41598-018-26566-3.

[21] S. I. Terada, K. Kobayashi, M. Ohkura, J. Nakai, and M. Matsuzaki, “Super-wide-field two-photon imaging with a micro-optical device moving in post-objective space,” *Nature Communications*, vol. 9, no. 1, 2018, doi: 10.1038/s41467-018-06058-8.

[22] N. J. Sofroniew, D. Flickinger, J. King, and K. Svoboda, “A large field of view two-photon mesoscope with subcellular resolution for in vivo imaging,” *eLife*, vol. 5, Jun. 2016, doi: 10.7554/eLife.14472.

[23] O. I. Rumyantsev *et al.*, “Fundamental bounds on the fidelity of sensory cortical

coding," *Nature*, vol. 580, no. 7801, pp. 100–105, 2020, doi: 10.1038/s41586-020-2130-2.

[24] S. Weisenburger *et al.*, "Volumetric Ca2+ Imaging in the Mouse Brain Using Hybrid Multiplexed Sculpted Light Microscopy," *Cell*, vol. 177, no. 4, pp. 1050-1066.e14, 2019, doi: 10.1016/j.cell.2019.03.011.

[25] J. Demas *et al.*, "Volumetric Calcium Imaging of 1 Million Neurons Across Cortical Regions at Cellular Resolution using Light Beads Microscopy," pp. 1–46, 2021.

[26] Z. S. Chen and B. Pesaran, "Improving scalability in systems neuroscience," *Neuron*, vol. 109, no. 11, pp. 1776–1790, 2021, doi: 10.1016/j.neuron.2021.03.025.

[27] J. Lecoq, N. Orlova, and B. F. Grewe, "Wide. Fast. Deep: Recent Advances in Multiphoton Microscopy of In Vivo Neuronal Activity," *The Journal of Neuroscience*, vol. 39, no. 46, pp. 9042–9052, Nov. 2019, doi: 10.1523/JNEUROSCI.1527-18.2019.

[28] P. J. Drew *et al.*, "Chronic optical access through a polished and reinforced thinned skull," *Nature Methods*, vol. 7, no. 12, pp. 981–984, 2010, doi: 10.1038/nmeth.1530.

[29] G. Yang, F. Pan, C. N. Parkhurst, J. Grutzendler, and W.-B. Gan, "Thinned-skull cranial window technique for long-term imaging of the cortex in live mice," *Nature Protocols*, vol. 5, no. 2, pp. 201–208, Feb. 2010, doi: 10.1038/nprot.2009.222.

[30] Y. J. Zhao *et al.*, "Skull optical clearing window for in vivo imaging of the mouse cortex at synaptic resolution," *Light: Science and Applications*, vol. 7, no. 2, p. 17153, 2018, doi: 10.1038/lsa.2017.153.

[31] C. Zhang *et al.*, "A large, switchable optical clearing skull window for

cerebrovascular imaging," *Theranostics*, vol. 8, no. 10, pp. 2696–2708, 2018, doi: 10.7150/thno.23686.

[32] G. J. Goldey *et al.*, "Removable cranial windows for long-term imaging in awake mice," *Nature Protocols*, vol. 9, no. 11, pp. 2515–2538, Nov. 2014, doi: 10.1038/nprot.2014.165.

[33] A. Holtmaat *et al.*, "Long-term, high-resolution imaging in the mouse neocortex through a chronic cranial window," *Nature Protocols*, vol. 4, no. 8, pp. 1128–1144, Aug. 2009, doi: 10.1038/nprot.2009.89.

[34] C. Heo *et al.*, "A soft, transparent, freely accessible cranial window for chronic imaging and electrophysiology," *Scientific Reports*, vol. 6, no. May, pp. 1–11, 2016, doi: 10.1038/srep27818.

[35] T. H. Kim *et al.*, "Long-Term Optical Access to an Estimated One Million Neurons in the Live Mouse Cortex," *Cell Reports*, vol. 17, no. 12, pp. 3385–3394, 2016, doi: 10.1016/j.celrep.2016.12.004.

[36] L. Ghanbari *et al.*, "Cortex-wide neural interfacing via transparent polymer skulls," *Nature Communications*, vol. 10, no. 1, p. 1500, Dec. 2019, doi: 10.1038/s41467-019-09488-0.

[37] K. Hagisawa *et al.*, "Effective control of massive venous bleeding by 'multioverlapping therapy' using polysaccharide nanosheets in a rabbit inferior vena cava injury model," *Journal of Vascular Surgery: Venous and Lymphatic Disorders*, vol. 1, no. 3, pp. 289–297, Jul. 2013, [Online]. Available: https://linkinghub.elsevier.com/retrieve/pii/S2213333X13000474

[38] Y. Okamura, K. Kabata, M. Kinoshita, D. Saitoh, and S. Takeoka, "Free-standing biodegradable poly(lactic acid) nanosheet for sealing operations in surgery,"

Advanced Materials, vol. 21, no. 43, pp. 4388–4392, Nov. 2009, doi: 10.1002/adma.200901035.

[39] T. Fujie *et al.*, "Sealing effect of a polysaccharide nanosheet for murine cecal puncture," *Surgery*, vol. 148, no. 1, pp. 48–58, Jul. 2010, doi: 10.1016/j.surg.2009.12.009.

[40] Y. Okamura *et al.*, "Fragmentation of Poly(lactic acid) nanosheets and patchwork treatment for burn wounds," *Advanced Materials*, vol. 25, no. 4, pp. 545–551, 2013, doi: 10.1002/adma.201202851.

[41] T. Komachi, H. Sumiyoshi, Y. Inagaki, S. Takeoka, Y. Nagase, and Y. Okamura, "Adhesive and robust multilayered poly(lactic acid) nanosheets for hemostatic dressing in liver injury model," *Journal of Biomedical Materials Research - Part B Applied Biomaterials*, vol. 105, no. 7, pp. 1747–1757, 2017, doi: 10.1002/jbm.b.33714.

[42] H. Zhang *et al.*, "Porous nanosheet wrapping for live imaging of suspension cells," *Journal of Materials Chemistry B*, 2018, doi: 10.1039/C8TB01943F.

[43] H. Zhang *et al.*, "Fluoropolymer Nanosheet as a Wrapping Mount for High-Quality Tissue Imaging," *Advanced Materials*, vol. 29, no. 37, p. 1703139, Oct. 2017, doi: 10.1002/adma.201703139.

[44] D. Someya, S. Arai, T. Fujie, and S. Takeoka, "Extracellular pH imaging of a plant leaf with a polyelectrolyte multilayered nanosheet †," 2018, doi: 10.1039/c8ra06308g.

[45] H. Zhang, K. Yarinome, R. Kawakami, K. Otomo, T. Nemoto, and Y. Okamura, "Nanosheet wrapping-assisted coverslip-free imaging for looking deeper into a tissue at high resolution," *PLOS ONE*, vol. 15, no. 1, p. e0227650, Jan. 2020, doi:

10.1371/journal.pone.0227650.

[46] T. Takahashi *et al.*, “PEO-CYTOP Fluoropolymer Nanosheets as a Novel Open-Skull Window for Imaging of the Living Mouse Brain,” *iScience*, vol. 23, no. 10, p. 101579, Oct. 2020, doi: 10.1016/j.isci.2020.101579.

[47] S. Zhang, Y. Sunami, and H. Hashimoto, “Mini Review: Nanosheet Technology towards Biomedical Application.,” *Nanomaterials (Basel, Switzerland)*, vol. 7, no. 9, Aug. 2017, doi: 10.3390/nano7090246.

[48] T. Miyagawa, T. Fujie, T. Thang Vo Doan, H. Sato, and S. Takeoka, “Glue-Free Stacked Luminescent Nanosheets Enable High-Resolution Ratiometric Temperature Mapping in Living Small Animals,” 2016, doi: 10.1021/acsami.6b06075.

[49] G. Feng *et al.*, “Imaging Neuronal Subsets in Transgenic Mice Expressing Multiple Spectral Variants of GFP,” *Neuron*, vol. 28, no. 1, pp. 41–51, Oct. 2000, doi: 10.1016/S0896-6273(00)00084-2.

[50] H. Monai *et al.*, “Calcium imaging reveals glial involvement in transcranial direct current stimulation-induced plasticity in mouse brain,” *Nature Communications*, vol. 7, pp. 1–10, 2016, doi: 10.1038/ncomms11100.

[51] H. Dana *et al.*, “High-performance calcium sensors for imaging activity in neuronal populations and microcompartments,” *Nature Methods*, vol. 16, no. 7, pp. 649–657, 2019, doi: 10.1038/s41592-019-0435-6.

[52] K. Iijima, T. Oshima, R. Kawakami, and T. Nemoto, “Optical clearing of living brains with MAGICAL to extend in vivo imaging,” *iScience*, vol. 24, no. 1, p. 101888, Jan. 2021, doi: 10.1016/j.isci.2020.101888.

[53] K. Haruwaka *et al.*, “Dual microglia effects on blood brain barrier permeability

induced by systemic inflammation," *Nature Communications*, vol. 10, no. 1, pp. 1–17, 2019, doi: 10.1038/s41467-019-13812-z.

[54] T. Takahashi, H. Zhang, K. Otomo, Y. Okamura, and T. Nemoto, "Protocol for constructing an extensive cranial window utilizing a PEO-CYTOP nanosheet for in vivo wide-field imaging of the mouse brain," *STAR Protocols*, vol. 2, no. 2, p. 100542, 2021, doi: 10.1016/j.xpro.2021.100542.

[55] N. Otsu, "A Threshold Selection Method from Gray-Level Histograms," *IEEE Transactions on Systems, Man, and Cybernetics*, vol. 9, no. 1, pp. 62–66, Jan. 1979, doi: 10.1109/TSMC.1979.4310076.

[56] A. Giovannucci *et al.*, "Caiman an open source tool for scalable calcium imaging data analysis," *eLife*, vol. 8, pp. 1–45, 2019, doi: 10.7554/eLife.38173.

[57] J. L. Stobart *et al.*, "Cortical Circuit Activity Evokes Rapid Astrocyte Calcium Signals on a Similar Timescale to Neurons," *Neuron*, vol. 98, no. 4, pp. 726-735.e4, 2018, doi: 10.1016/j.neuron.2018.03.050.

[58] K. Yamaguchi *et al.*, "Adaptive Optical Two-Photon Microscopy for Surface-Profiled Living Biological Specimens," *ACS Omega*, p. acsomega.0c04888, Nov. 2020, doi: 10.1021/acsomega.0c04888.

[59] K. Yamaguchi, R. Kitamura, R. Kawakami, K. Otomo, and T. Nemoto, "In vivo two-photon microscopic observation and ablation in deeper brain regions realized by modifications of excitation beam diameter and immersion liquid," *PLoS ONE*, vol. 15, no. 8 August, pp. 1–18, 2020, doi: 10.1371/journal.pone.0237230.

[60] Y. Ue *et al.*, "A spherical aberration-free microscopy system for live brain imaging," *Biochemical and Biophysical Research Communications*, vol. 500, no. 2, pp. 236–241, Jun. 2018, doi: 10.1016/J.BBRC.2018.04.049.

[61] N. Matsumoto, A. Konno, T. Inoue, and S. Okazaki, “Aberration correction considering curved sample surface shape for non-contact two-photon excitation microscopy with spatial light modulator,” *Scientific Reports*, vol. 8, no. 1, pp. 1–13, 2018, doi: 10.1038/s41598-018-27693-7.

[62] A. Tanabe *et al.*, “Transmissive liquid-crystal device for correcting primary coma aberration and astigmatism in biospecimen in two-photon excitation laser scanning microscopy,” *Journal of Biomedical Optics*, vol. 21, no. 12, p. 121503, 2016, doi: 10.1117/1.jbo.21.12.121503.

[63] G. J. Goldey *et al.*, “Removable cranial windows for long-term imaging in awake mice,” *Nature Protocols*, vol. 9, no. 11, pp. 2515–2538, Nov. 2014, doi: 10.1038/nprot.2014.165.

[64] M. Roche, E. Chaigneau, R. L. Rungta, D. Boido, B. Weber, and S. Charpak, “In vivo imaging with a water immersion objective affects brain temperature, blood flow and oxygenation,” *eLife*, vol. 8, pp. 1–12, 2019, doi: 10.7554/eLife.47324.

[65] V. A. Griffiths *et al.*, “Real-time 3D movement correction for two-photon imaging in behaving animals,” *Nature Methods*, vol. 17, no. 7, pp. 741–748, 2020, doi: 10.1038/s41592-020-0851-7.

[66] D. Karagyozov, M. Mihovilovic Skanata, A. Lesar, and M. Gershow, “Recording Neural Activity in Unrestrained Animals with Three-Dimensional Tracking Two-Photon Microscopy,” *Cell Reports*, vol. 25, no. 5, pp. 1371-1383.e10, 2018, doi: 10.1016/j.celrep.2018.10.013.

[67] M. Strathmann, A. P. Leis, S. Schlicher, and H. Franke, “Optically Transparent Porous Medium for Nondestructive Studies of Microbial Bio lm Architecture and Transport Dynamics,” *Applied and Environmental Microbiology*, vol. 71, no. 8, pp.

4801–4808, 2005, doi: 10.1128/AEM.71.8.4801.

[68] Y. Ikeda and Y. Nagasaki, “Impacts of PEGylation on the gene and oligonucleotide delivery system,” *Journal of Applied Polymer Science*, vol. 131, no. 9, pp. 1–10, 2014, doi: 10.1002/app.40293.

[69] A. Y. Shih, J. D. Driscoll, P. J. Drew, N. Nishimura, C. B. Schaffer, and D. Kleinfeld, “Two-Photon Microscopy as a Tool to Study Blood Flow and Neurovascular Coupling in the Rodent Brain,” *Journal of Cerebral Blood Flow & Metabolism*, vol. 32, no. 7, pp. 1277–1309, Jul. 2012, doi: 10.1038/jcbfm.2011.196.

[70] J. A. Coles, P. J. Stewart-Hutchinson, E. Myburgh, and J. M. Brewer, “The mouse cortical meninges are the site of immune responses to many different pathogens, and are accessible to intravital imaging,” *Methods*, vol. 127, pp. 53–61, 2017, doi: 10.1016/j.ymeth.2017.03.020.

[71] A. Arieli, A. Grinvald, and H. Slovin, “Dural substitute for long-term imaging of cortical activity in behaving monkeys and its clinical implications,” *Journal of Neuroscience Methods*, vol. 114, no. 2, pp. 119–133, 2002, doi: 10.1016/S0165-0270(01)00507-6.

[72] N. Jackson and J. Muthuswamy, “Artificial dural sealant that allows multiple penetrations of implantable brain probes.,” *Journal of neuroscience methods*, vol. 171, no. 1, pp. 147–52, Jun. 2008, doi: 10.1016/j.jneumeth.2008.02.018.

[73] U. Gimsa *et al.*, “Optimizing a rodent model of parkinson’s disease for exploring the effects and mechanisms of deep brain stimulation,” *Parkinson’s Disease*, vol. 2011, 2011, doi: 10.4061/2011/414682.

[74] D. D. Stettler, H. Yamahachi, W. Li, W. Denk, and C. D. Gilbert, “Axons and synaptic boutons are highly dynamic in adult visual cortex,” *Neuron*, vol. 49, no.

6, pp. 877–887, 2006, doi: 10.1016/j.neuron.2006.02.018.

[75] A. Klioutchnikov *et al.*, “Three-photon head-mounted microscope for imaging deep cortical layers in freely moving rats,” *Nature Methods*, vol. 17, no. 5, pp. 509–513, 2020, doi: 10.1038/s41592-020-0817-9.

[76] S. Iwano *et al.*, “Single-cell bioluminescence imaging of deep tissue in freely moving animals,” *Science*, vol. 359, no. 6378, pp. 935–939, Feb. 2018, doi: 10.1126/science.aaq1067.

[77] S. Inagaki *et al.*, “In vivo brain activity imaging of interactively locomoting mice,” *bioRxiv*, pp. 1–34, 2017, doi: 10.1101/203422.

[78] N. Perentos, A. U. Nicol, A. Q. Martins, J. E. Stewart, P. Taylor, and A. J. Morton, “Techniques for chronic monitoring of brain activity in freely moving sheep using wireless EEG recording,” *Journal of Neuroscience Methods*, vol. 279, pp. 87–100, 2017, doi: 10.1016/j.jneumeth.2016.11.010.

[79] P. Gutruf and J. A. Rogers, “Implantable, wireless device platforms for neuroscience research,” *Current Opinion in Neurobiology*, vol. 50, pp. 42–49, 2018, doi: 10.1016/j.conb.2017.12.007.

Figure

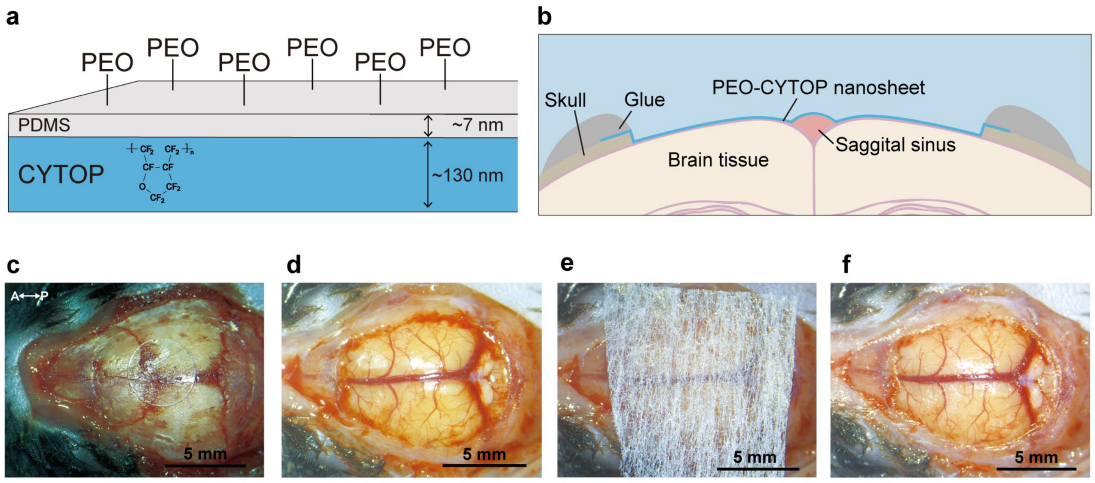

Figure 1 Application of the PEO-CYTOP Nanosheet to the Cranial Window

a. Schematic illustration of the PEO-CYTOP nanosheet. The upper side is the adhesive surface.

b. Schematic illustration of the cranial window utilizing the PEO-CYTOP nanosheet.

c. Skull view after the removal of the hair and scalp and placement of a glass coverslip with a diameter of 4.2 mm. The directions are indicated as anterior (A), posterior (P).

d. Exposure of the brain tissues after the removal of the cranial skull, with preservation of the dura.

e. The PEO-CYTOP nanosheet on the nonwoven fabric was placed on the brain surface.

f. Cranial window sealed with the PEO-CYTOP nanosheet.

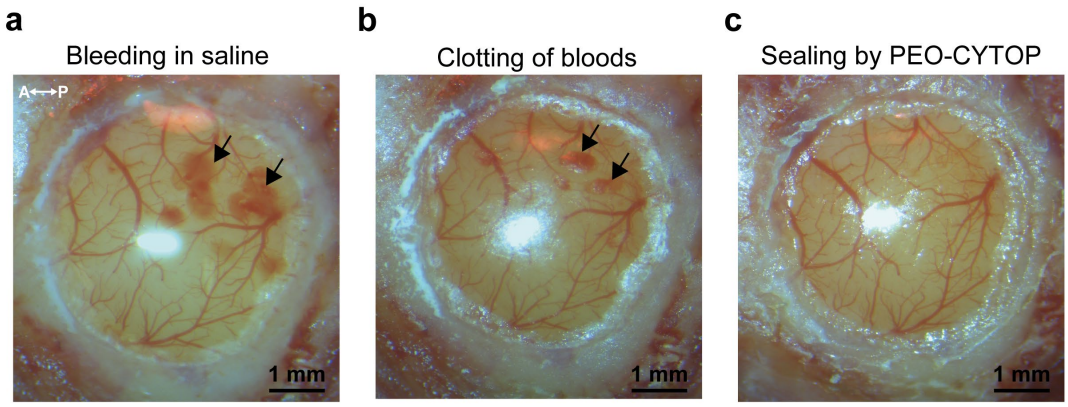

Figure 2 The Suppression of Bleeding and Clotting of Blood with the PEO-CYTOP Nanosheet

a. Bleeding from the brain surface to saline after removing the skull. Arrows indicate the bleeding sites. The directions are indicated as anterior (A), posterior (P).

b. The clotting of blood on the surface in the same mouse as in Figure 2a. Arrows indicate the clotting sites.

c. The cranial window sealed by the PEO-CYTOP nanosheet in the same mouse without bleeding and coagulation of blood after washing the coagulation shown in Figure 2b.

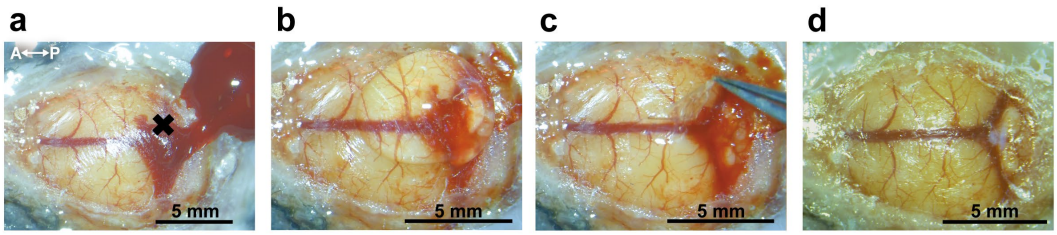

Figure 3 The Procedure of the Removal and Resealing of the PEO-CYTOP Nanosheet Intentionally Injuring the Right Transverse Sinus

a. Intentionally injuring the right transverse sinus with a needle. A black cross indicates the injured site. The directions are indicated as anterior (A), posterior (P).

b. Pouring saline into the broken PEO-CYTOP nanosheet to wash the blood from the injured site.

c. Removing the broken PEO-CYTOP nanosheet using tweezers.

d. Resealing the cranial window with another PEO-CYTOP nanosheet after washing the blood on the brain surface.

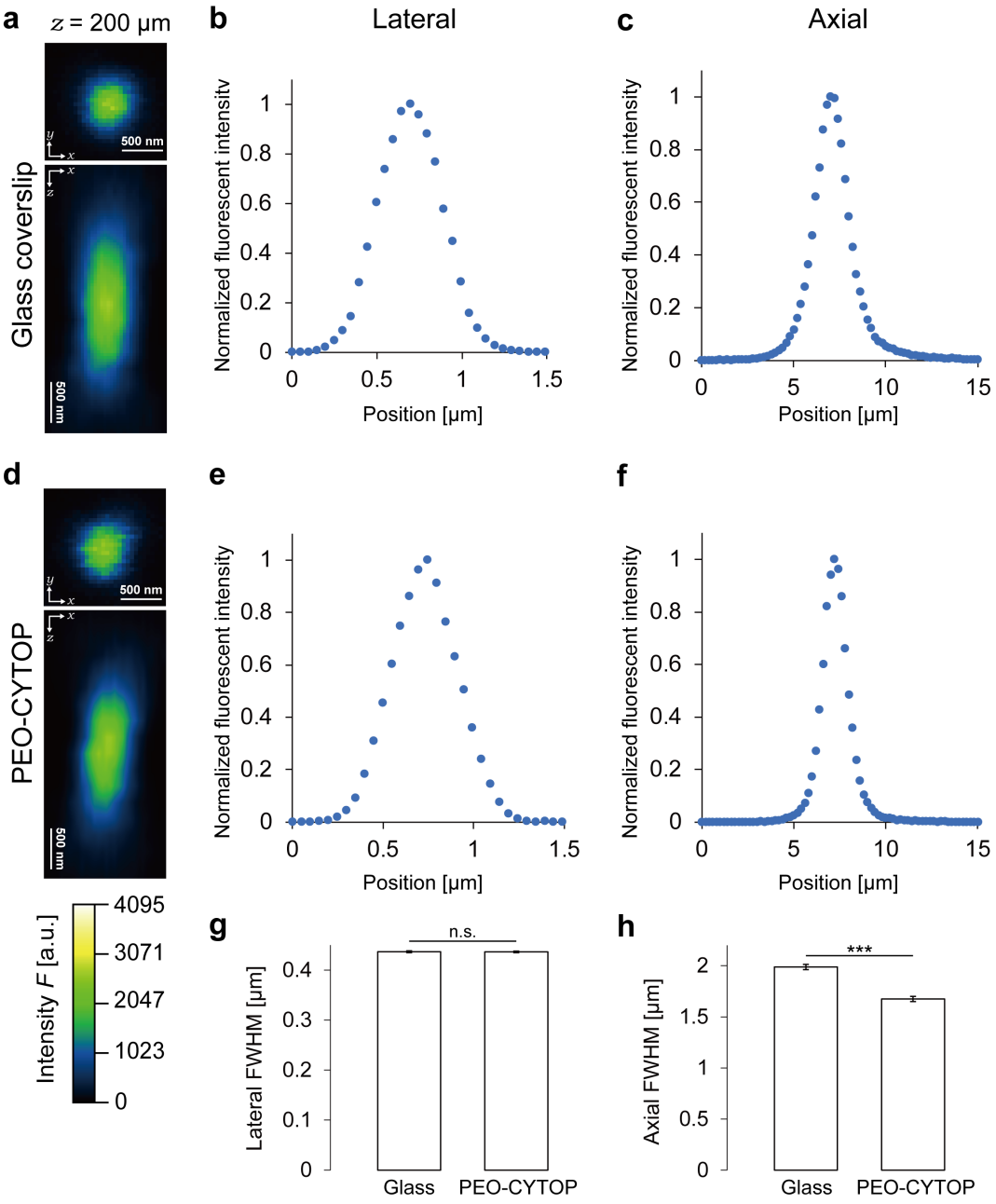

Figure 4 Comparison of the Axial and Lateral Resolution Between the PEO-CYTOP Nanosheet and a Glass Coverslip

a. Fluorescent images of 200-nm yellow-green beads using a glass coverslip in *xy* (top) and *xz* (bottom).

b. Lateral normalized fluorescence intensity of 200-nm yellow-green beads using glass coverslip.

c. Axial normalized fluorescence intensity of 200-nm yellow-green beads using glass coverslip.

d. Fluorescent images of 200-nm yellow-green beads using a PEO-CYTOP nanosheet in *xy* (top) and *xz* (bottom).

e. Lateral normalized fluorescence intensity of 200-nm yellow-green beads using a PEO-CYTOP nanosheet.

e. Axial normalized fluorescence intensity of 200-nm yellow-green beads using a PEO-CYTOP nanosheet.

f. The averaged axial FWHMs measured from the intensity profiles of the beads images obtained through each glass coverslip and PEO-CYTOP nanosheet; *: $p < 0.05$; **: $p < 0.01$; ***: $p < 0.005$ (Welch's t-test). Error bars represent standard error of the mean.

g. The averaged lateral FWHMs measured from the intensity profiles of the beads images obtained through each glass coverslip and PEO-CYTOP nanosheet; *: $p < 0.05$; **: $p < 0.01$; ***: $p < 0.005$ (Welch's t-test). Error bars represent standard error of the mean.

h. The averaged l FWHMs measured from the intensity profiles of the beads images obtained through each glass coverslip and PEO-CYTOP nanosheet; *: $p < 0.05$; **: $p < 0.01$; ***: $p < 0.005$ (Welch's t-test). Error bars represent standard error of the mean.

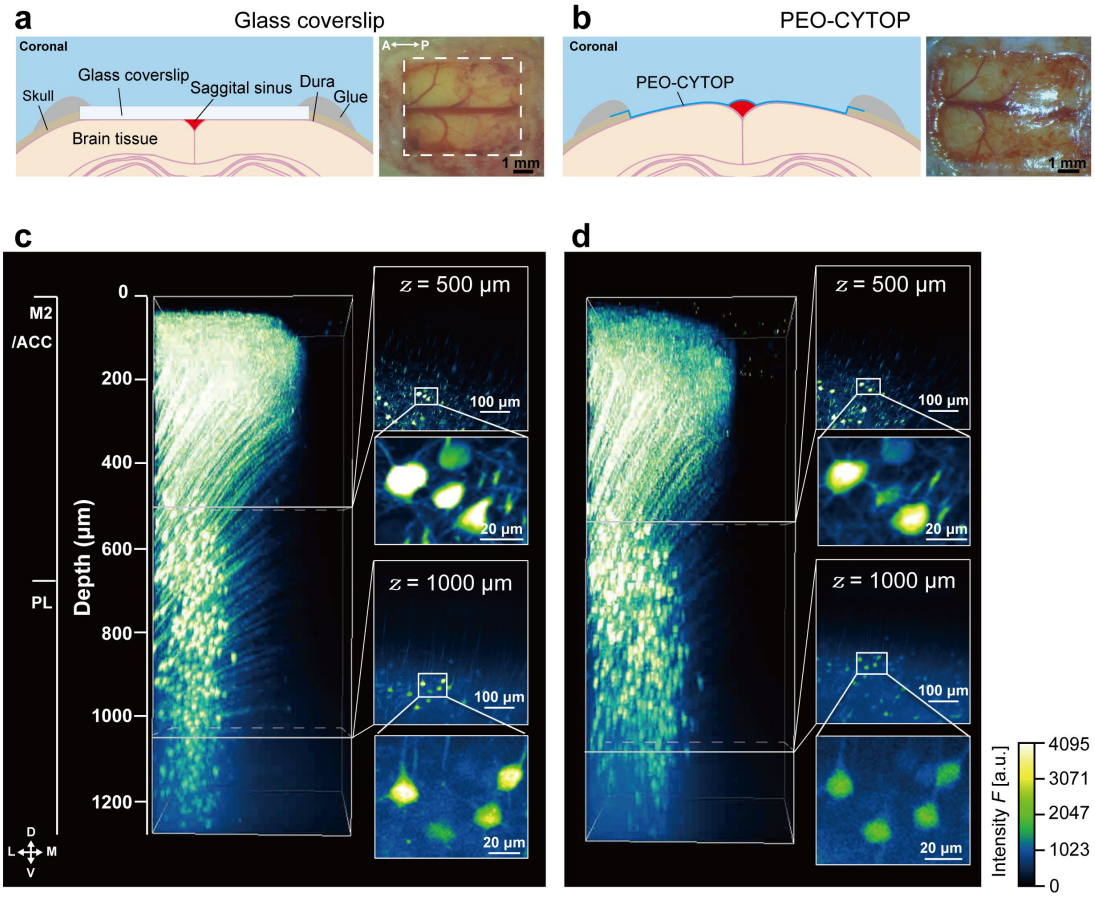

Figure 5 ***In Vivo*** **Two-Photon Imaging Using the PEO-CYTOP Nanosheet and a Glass Coverslip, In Turn**

a. The cranial window sealed with a glass coverslip on the parietal cortex in the adult H-line mouse brain. The directions are indicated as anterior (A), posterior (P). The white dotted line indicates the edge of the cranial window using a rectangular glass coverslip.

b. The cranial window sealed with a PEO-CYTOP nanosheet on the parietal cortex in the adult H-line mouse brain.

c. Maximum intensity projections of the two-photon fluorescent images of PFC neurons with the glass coverslip. M2, Secondary motor cortex; ACC, anterior

cingulate cortex; PL, prelimbic cortex. The directions are indicated as dorsal (D), ventral (V), medial (M), and lateral (L).

d. Maximum intensity projections of the two-photon fluorescent images of PFC neurons of the mouse with the PEO-CYTOP nanosheet.

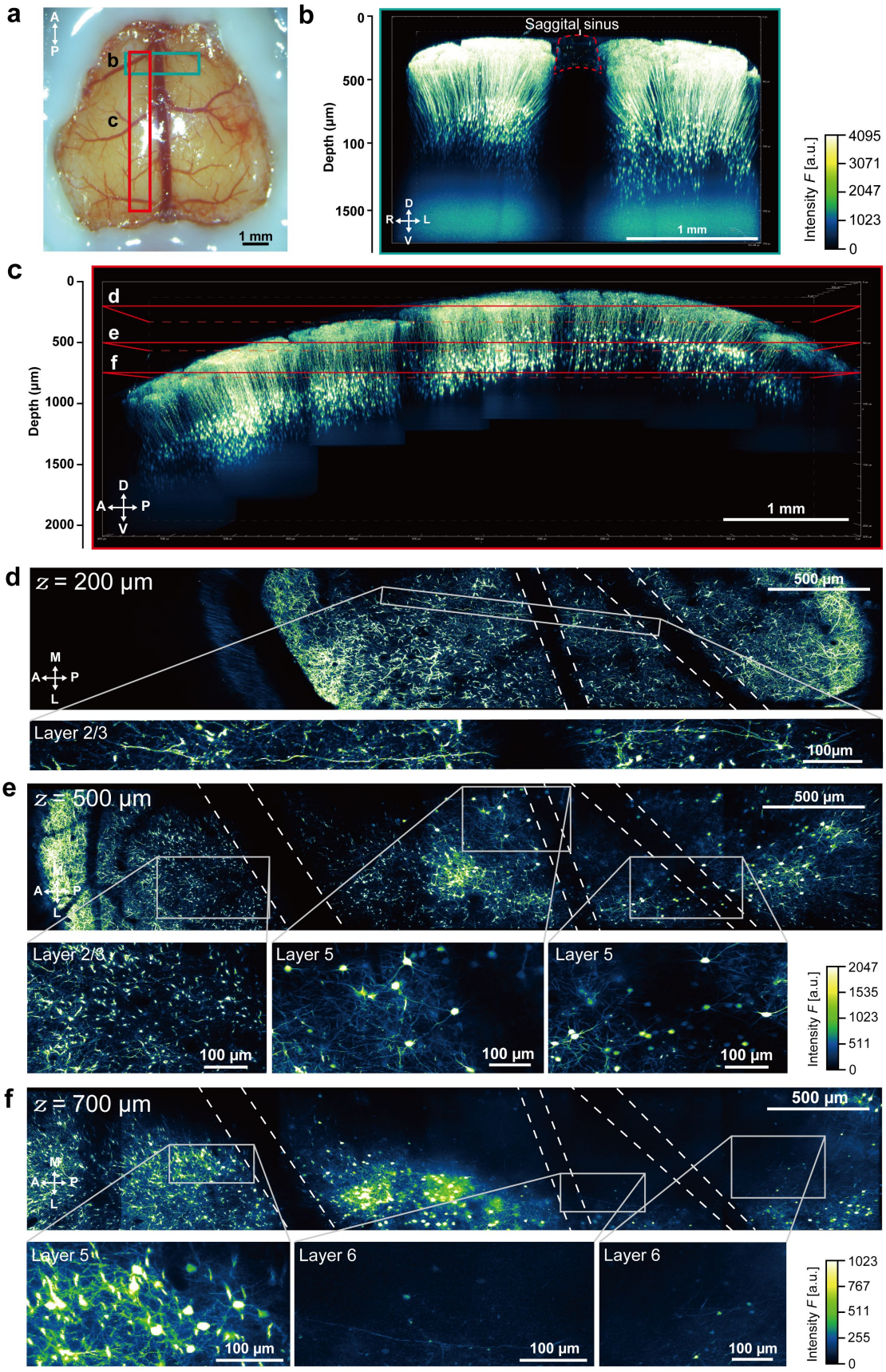
a
A
P
b
c
1 mm
b
Saggital sinus
0
500
100
1500
Depth (μm)
D
R
L
V
1 mm
Intensity F [a.u.]
4095
3071
2047
1023
0
c
d
e
f
0
500
1000
1500
2000
Depth (μm)
D
A
P
V
1 mm
d
z = 200 μm
500 μm
M
A
P
L
Layer 2/3
100μm
e
z = 500 μm
500 μm
Layer 2/3
Layer 5
Layer 5
100 μm
100 μm
100 μm
Intensity F [a.u.]
2047
1535
1023
511
0
f
z = 700 μm
500 μm
Layer 5
Layer 6
Layer 6
100 μm
100 μm
100 μm
Intensity F [a.u.]
1023
767
511
255
0

Figure 6 *In Vivo* Two-Photon Imaging in Thy1-EYFP-H Mice with a Cranial Window Using the PEO-CYTOP Nanosheet

a. Photo of the cranial window utilizing a PEO-CYTOP nanosheet in an H-line mouse. The regions within the green and red boxes are shown in detail in Figure 6b and c, respectively. The directions are indicated as anterior (A), posterior (P).

b. Tomographic images tiled with the maximum intensity projections of the three-dimensional stacks as a coronal section of the green box in Figure 6a. The dotted lines roughly correspond to the surface of the sagittal sinus. The directions are indicated as dorsal (D), ventral (V), right (R), and left (L).

c. Tomographic images tiled with the maximum intensity projections of the three-dimensional stacks as a sagittal section of the red box in Figure 6a. The red lines indicate the section of Figure 6d–f. The directions are indicated as dorsal (D), ventral (V), anterior (A), and posterior (P).

d. Cross-sectional *xy*-images of the axons or apical dendrites from the region located at a depth of 200 μm from the surface, as illustrated in Figure 6c. The dotted line indicates the invisible area under blood vessels.

e. Cross-sectional *xy*-images of the pyramidal cell bodies or apical dendrites from the region located at a depth of 500 μm from the surface, as illustrated in Figure 6c. The dotted line indicates the invisible area under blood vessels.

f. Cross-sectional *xy*-images of the pyramidal cell bodies from the region located at a depth of 700 μm from the surface, as illustrated in Figure 6c. The dotted line indicates the invisible area under blood vessels.

The directions are indicated as anterior (A), posterior (P), medial (M), and lateral (L) in d, e, f.

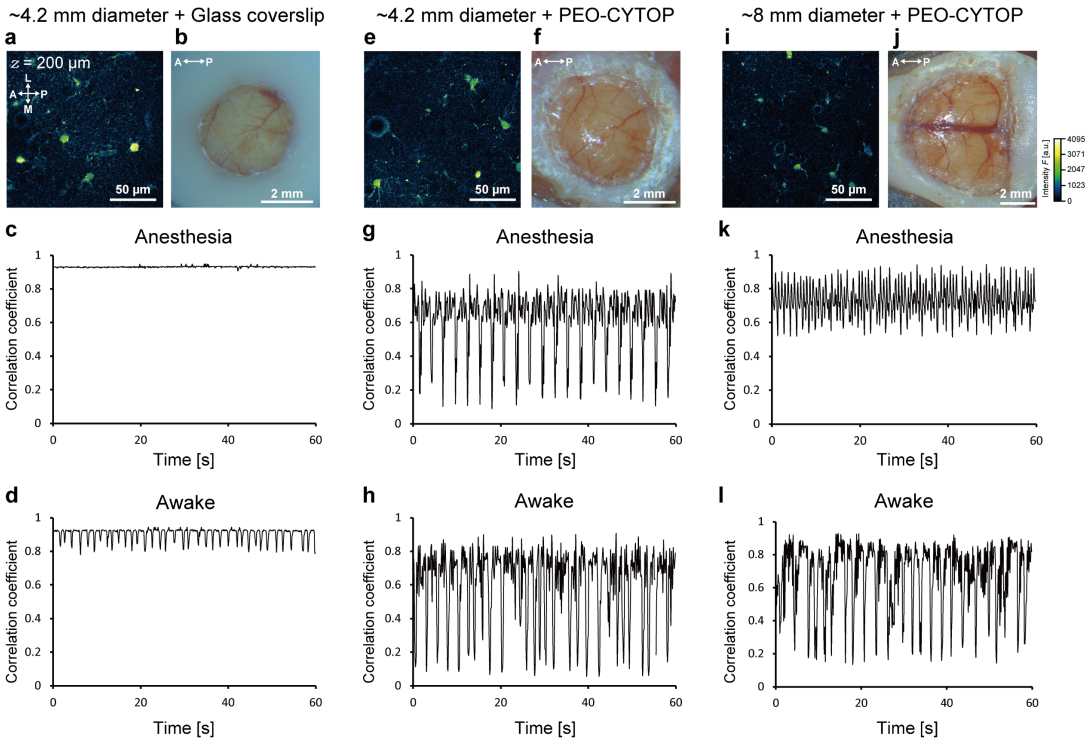

Figure 7 Evaluation of Motion Artifacts in Anesthetized and Awake Mouse Utilizing a PEO-CYTOP Nanosheet

a. An example image of two-photon imaging of astrocytes labeled with Sulforhodamine 101 (SR101) with a small cranial window of a glass coverslip. The directions are indicated as anterior (A), posterior (P), medial (M), and lateral (L).

b. A small cranial window sealed by glass coverslip on the V1 area in the brain of an adult wild-type mouse. The directions are indicated as anterior (A), posterior (P).

c. Time series of a correlation coefficient calculated from each frame in the anesthetized condition of the same mouse as Figure 7a.

d. Time series of a correlation coefficient calculated from each frame in the awake condition of the same mouse as Figure 7a.

e. An example image of two-photon imaging of astrocytes labeled with SR101 with a small cranial window of a PEO-CYTOP nanosheet.

f. A small cranial window sealed with a PEO-CYTOP nanosheet on the V1 area in the adult WT mouse brain. The directions are indicated as anterior (A), posterior (P).

g. Time series of a correlation coefficient calculated from each frame in the anesthetized condition of the same mouse as Figure 7e.

h. Time series of a correlation coefficient calculated from each frame in the awake condition of the same mouse as Figure 7e.

i. An example image of two-photon imaging of astrocytes labeled with SR101 with a large cranial window of PEO-CYTOP nanosheet.

j. Large cranial window sealed by a PEO-CYTOP nanosheet on the parietal cortex in the adult WT mouse brain. The directions are indicated as anterior (A), posterior (P).

k. Time series of correlation coefficients calculated from each frame in the same mouse as Figure 7i, under anesthesia.

l. The graph of time series of a correlation coefficient calculated from each frame in the awake condition of the same mouse as Figure 7i.

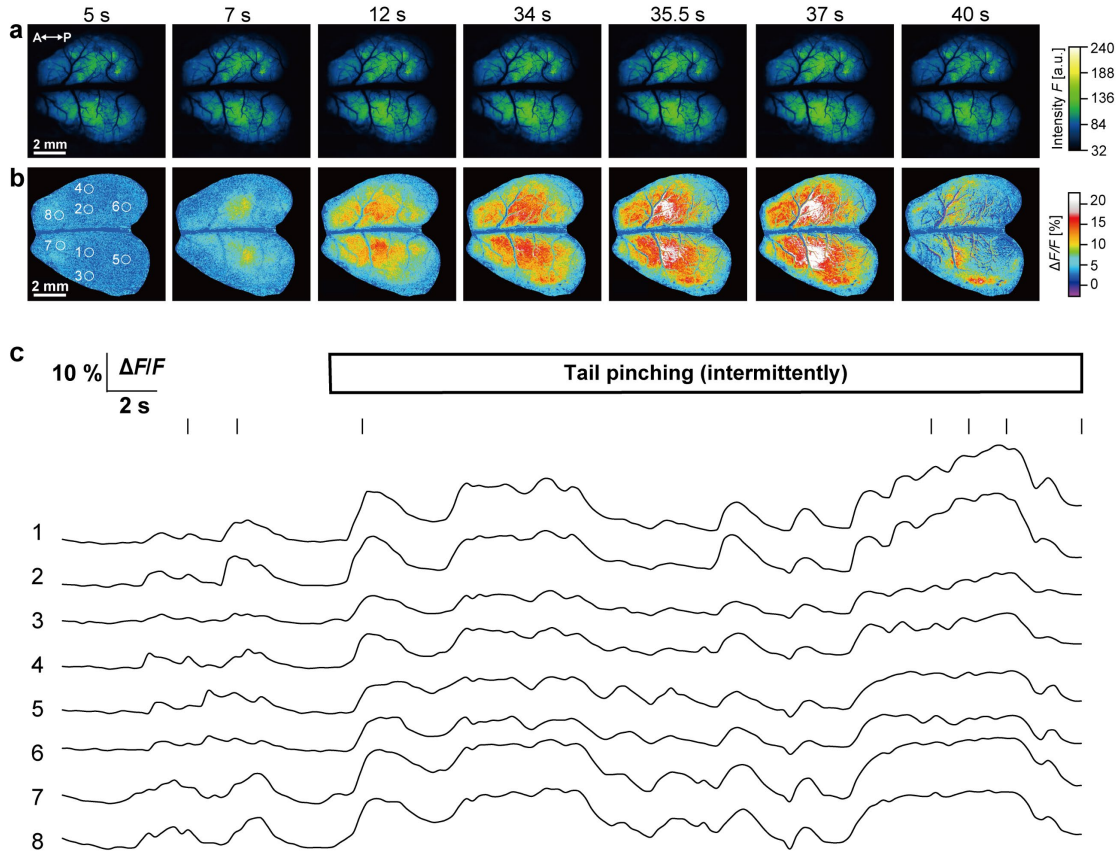

Figure 8 Wide-Field Imaging of GLT1-G-CaMP7 Mouse Utilizing the PEO-CYTOP Nanosheet

a. Time-lapse fluorescent images of Ca^{2+} elevations in the mouse. The times are indicated using short solid lines in Figure 8c.

b. Time-lapse images of fluorescence intensity change before and after tail pinching intermittently. The times are indicated using short solid lines in Figure 8c. The red circles and white numbers represent the ROIs for fluorescent intensity traces in Figure 8c.

c. Relative fluorescence intensity change ($\Delta F/F$) traces from the ROIs of Figure 8b. The short solid lines indicate the time of Figure 8b. In the second half of the trace, stimulation was applied by tail pinching approximately once a second.

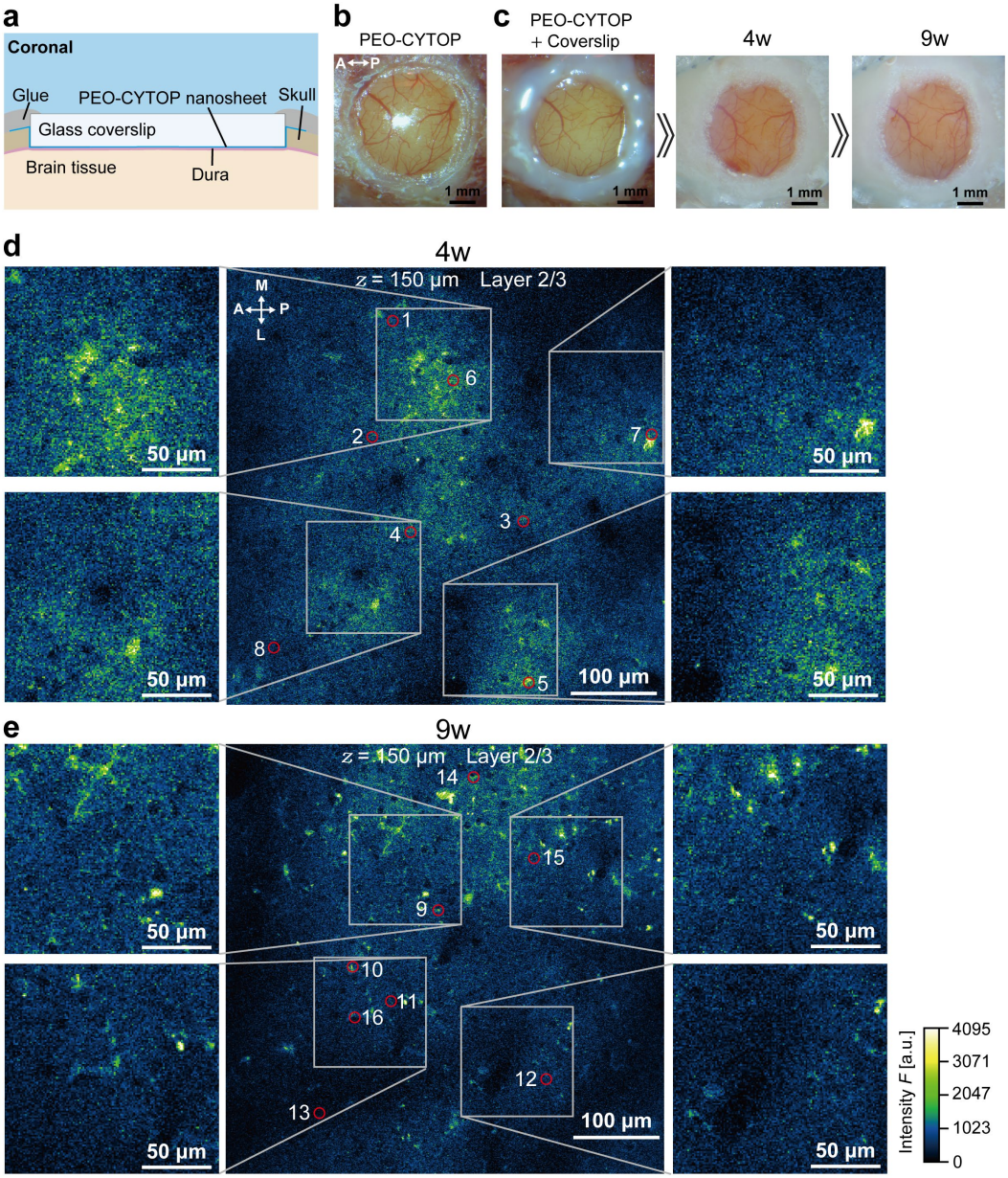
a
Coronal
Glue
PEO-CYTOP nanosheet
Skull
Glass coverslip
Brain tissue
Dura
b
PEO-CYTOP
A↔P
1 mm
c
PEO-CYTOP
+ Coverslip
4w
9w
1 mm
d
4w
z = 150 µm Layer 2/3
M
A
P
L
1
6
2
7
3
4
8
5
50 µm
100 µm
e
9w
z = 150 µm Layer 2/3
14
15
9
10
11
16
12
13
Intensity F [a.u.]
4095
3071
2047
1023
0
f
4w
Astrocytes
Neurons
1
2
3
4
5
6
7
8
g
9w
50 %
ΔF/F
5 s
Astrocytes
Neurons
9
10
11
12
13
14
15
16

Figure 9 *In Vivo* Two-Photon Imaging of GLT1-G-CaMP7 Mouse with the PEO-CYTOP Nanosheet

a. Schematic illustration of the cranial window utilizing the PEO-CYTOP nanosheet combined with a glass coverslip on the primary visual cortex (V1).

b. Photo of the cranial window utilizing the PEO-CYTOP nanosheet on the V1 in a G7NG817 mouse immediately after surgery. The directions are indicated as anterior (A), posterior (P).

c. Photos of the cranial window of Figure 9b sealed with a glass coverslip up to 9 weeks after surgery.

d. Fluorescent images of Ca^{2+} elevations in the primary visual cortex layer 2/3 at 4 weeks after surgery in the same mouse as Figure 9c. The red circle and white numbers represent the ROIs used for the fluorescent intensity traces depicted in Figure 9f. Medial (M), lateral (L), anterior (A), and posterior (P) directions.

e. Fluorescent images of Ca^{2+} elevations in the primary visual cortex layer 2/3 at 9 weeks after surgery in the same mouse as Figure 9c. The red circle and white numbers represent the ROIs used for the fluorescent intensity traces depicted in Figure 9g. Medial (M), lateral (L), anterior (A), and posterior (P) directions.

f. Relative fluorescence change ($\Delta F/F$) traces of Ca^{2+} transients from the ROIs depicted in Figure 9d. The numbers represent the ROIs shown in Figure 9d.

g. Relative fluorescence change ($\Delta F/F$) traces of Ca^{2+} transients from the ROIs depicted in Figure 9e. The numbers represent the ROIs shown in Figure 9e.

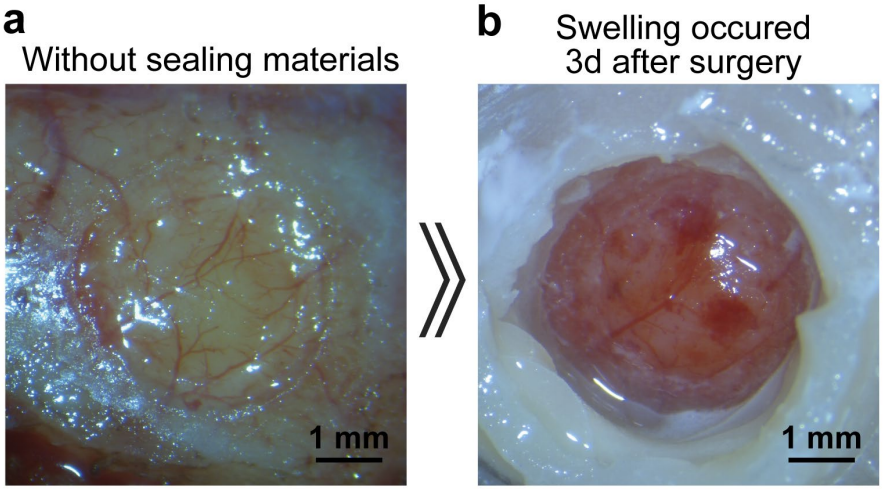

Figure 10 Swelling of the Brain Tissue Without Sealing Materials on the Surface

a. Photo of the cranial window without sealing materials in a diameter of 3.5 mm immediately after surgery.

b. Photo of the cranial window shown in Figure 10a, 3 days after surgery. The brain tissue was protected by a glass coverslip without directly touching the brain surface.

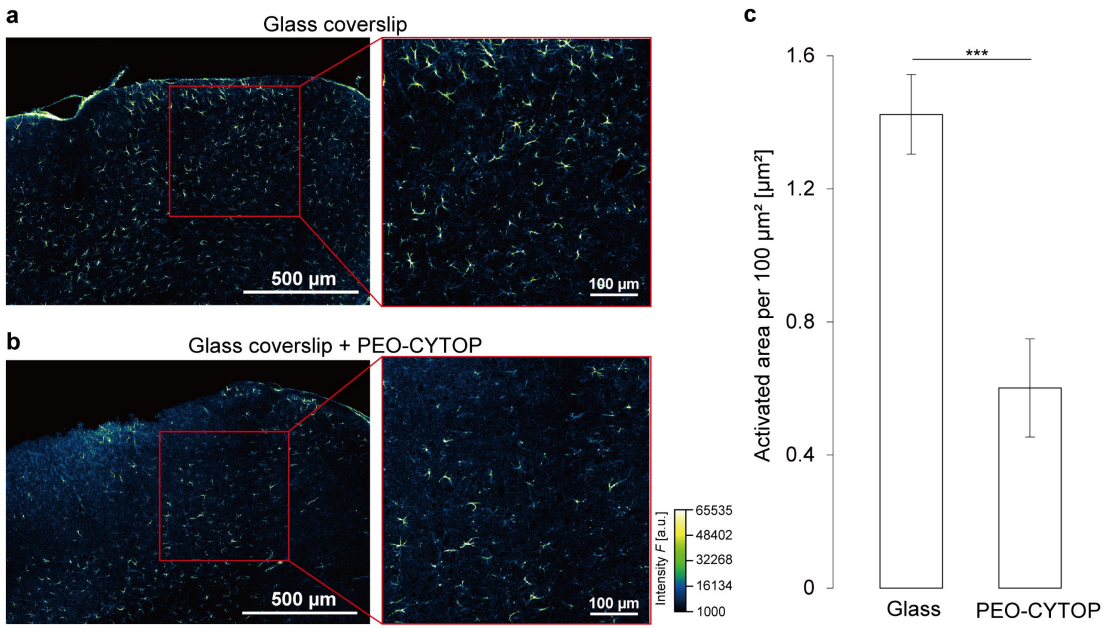

Figure 11 Evaluation of Inflammation in the Brain Tissue Underneath Cranial Windows Utilizing the PEO-CYTOP Nanosheet

a. Immunostaining of anti-GFAP in a mouse with a cranial window using glass coverslip 2 weeks after surgery.

b. Immunostained image of anti-GFAP in a mouse with a cranial window utilizing PEO-CYTOP nanosheet 2 weeks after surgery.

c. Bar plots indicating the activated area of astrocytes per 100 µm^2 in both cases using glass coverslip and PEO-CYTOP; *: $p < 0.05$; **: $p < 0.01$; ***: $p < 0.005$ (Welch's t-test). Error bars represent standard error of the mean.

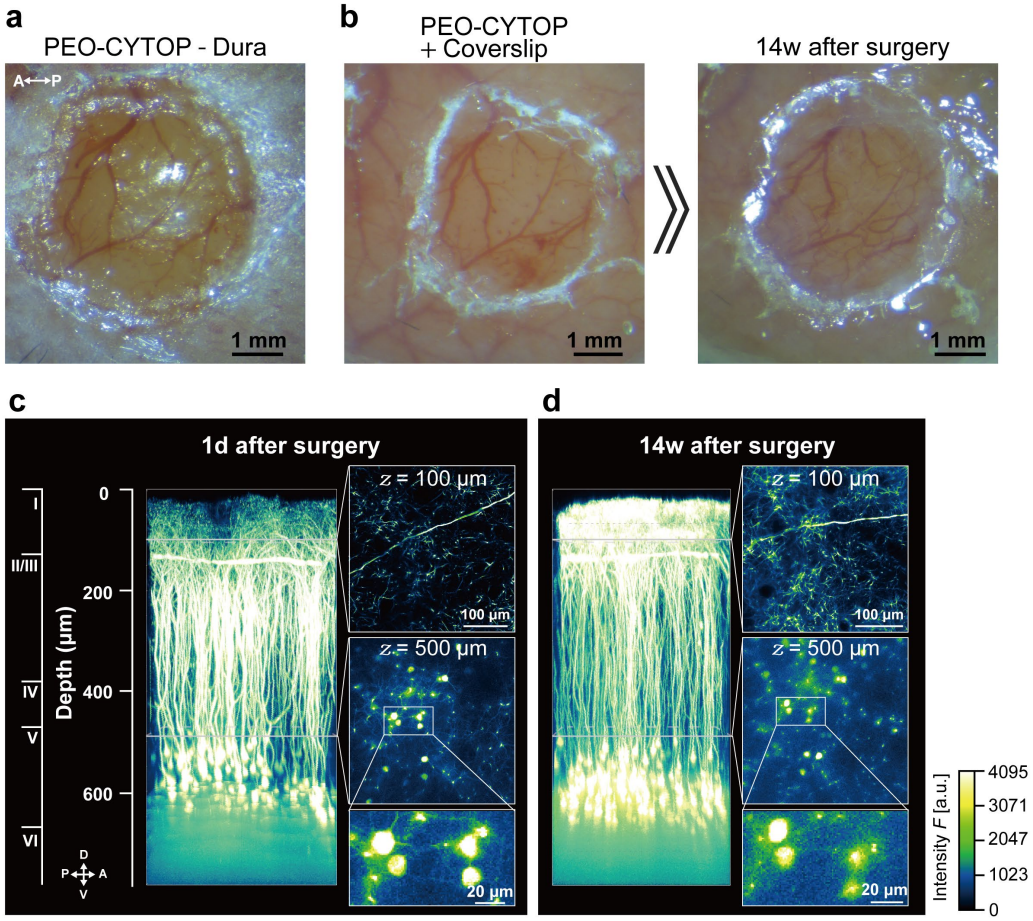

Figure 12 ***In Vivo*** **Two-Photon Imaging Utilizing the PEO-CYTOP Nanosheet with the Removal of the Dura**

a. Photo of the cranial window using the PEO-CYTOP nanosheet on the visual cortex (V1) in the H-line mouse. The directions are indicated as anterior (A), posterior (P).

b. Photos of the cranial window using the combination of the PEO-CYTOP nanosheet with a glass coverslip in the same mouse as Figure 12a, up to 14 weeks after surgery.

c. Maximum intensity projections of the two-photon fluorescent images in the same mouse as that shown in Figure 12b at 1 day after surgery. The directions are indicated as anterior dorsal (D), ventral (V), anterior (A), and posterior (P).

d. Maximum intensity projections of the two-photon fluorescent images in the same mouse as that used in Figure 12b at 14 weeks after surgery.

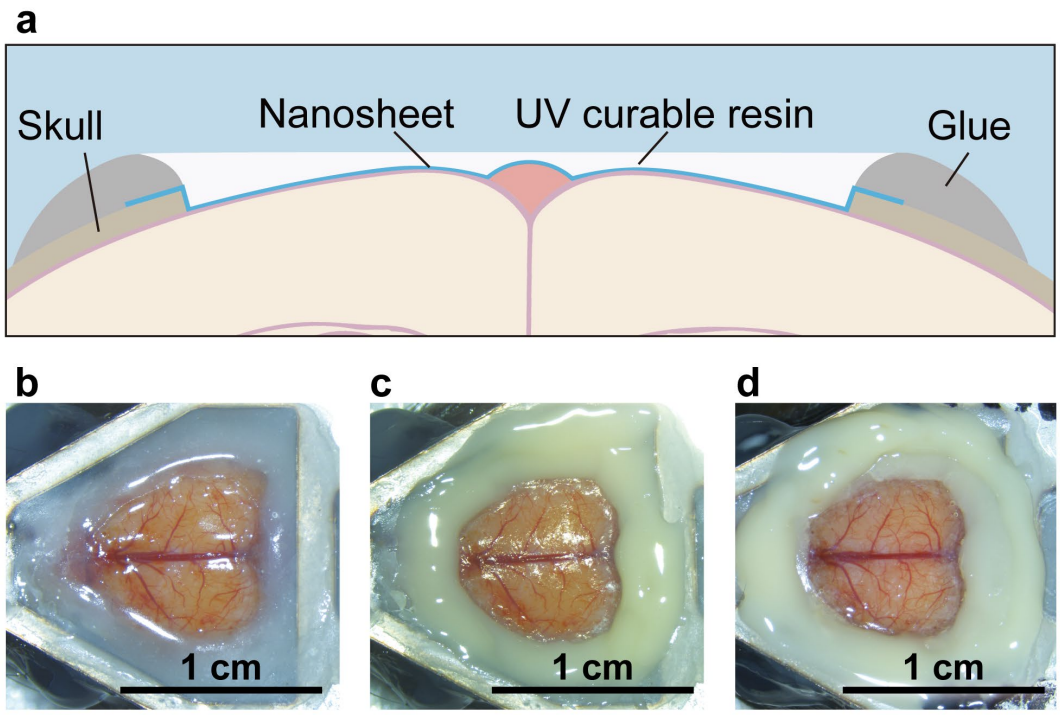

Figure 13 Application of the NIRE Method to Make the Cranial Window Combined with the PEO-CYTOP Nanosheet and UV Curable Resin

a. Schematic illustration of the cranial window covered by the PEO-CYTOP nanosheet and UV curable resin.

b. Exposure of the brain tissues after the removal of the cranial skull left the dura intact.

c. Sealing the brain surface with the PEO-CYTOP nanosheet.

d. Fixing UV curable resin on the PEO-CYTOP nanosheet.

a

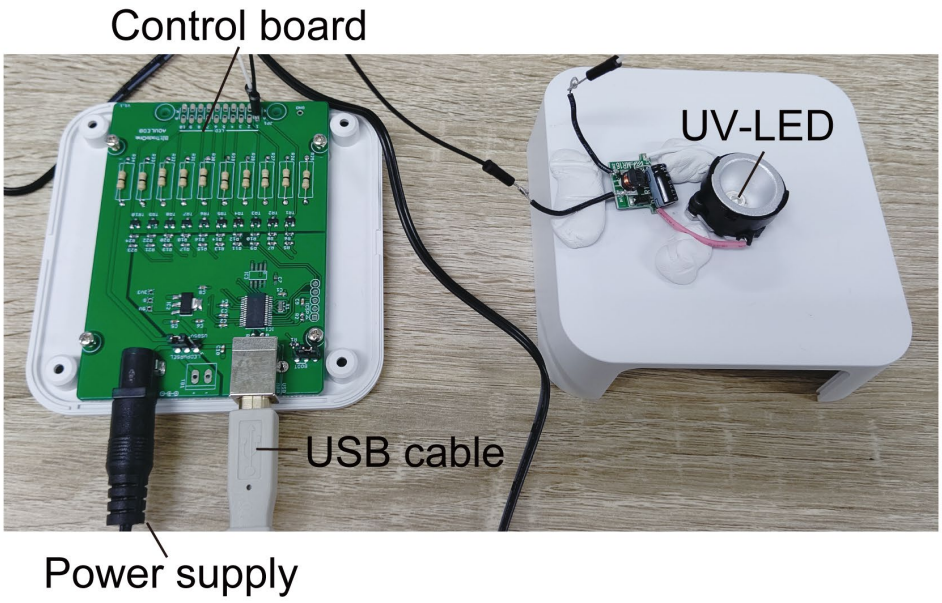
Control board
UV-LED
USB cable
Power supply

b

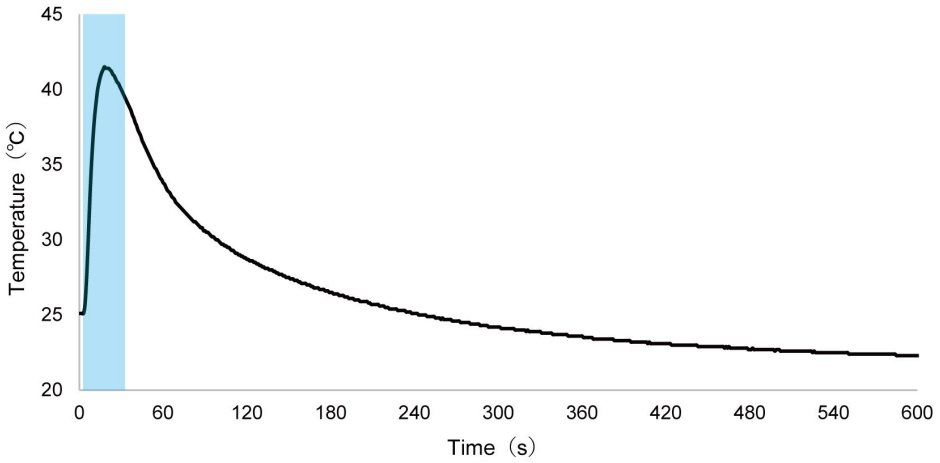
45
40
35
30
25
20
Temperature（℃）
0
60
120
180
240
300
360
420
480
540
600
Time（s）

c

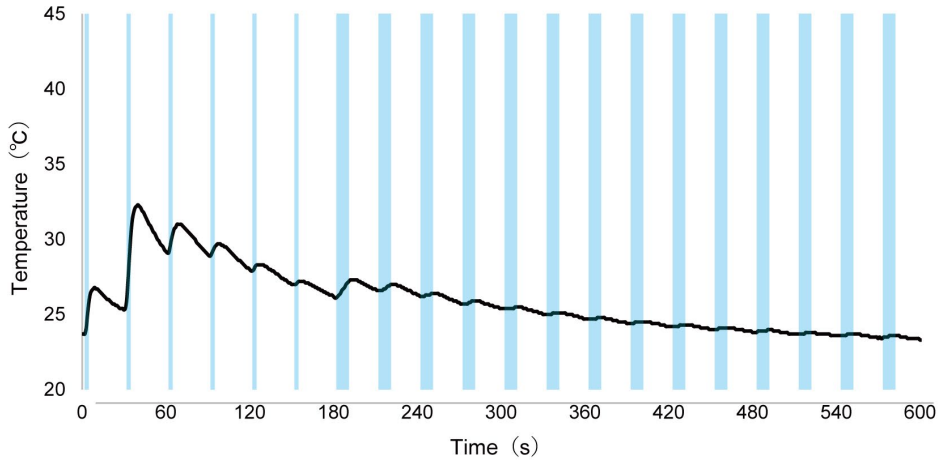
45
40
35
30
25
20
Temperature（℃）
0
60
120
180
240
300
360
420
480
540
600
Time（s）

Figure 14 Time and Power Programmable UV Irradiation System

a. Photo of handmade programmable UV irradiator.

b. Temperature change in 30 seconds of continuous UV irradiation to UV curable resin. The blue bar indicated the timing of UV irradiation.

c. Temperature change in intermittent UV irradiation. UV was irradiated to the UV curable resin at intervals of 2 seconds every 30 seconds for 3 minutes and 10 seconds every 30 seconds for 7 minutes. Blue bars indicated the timing of UV irradiation.

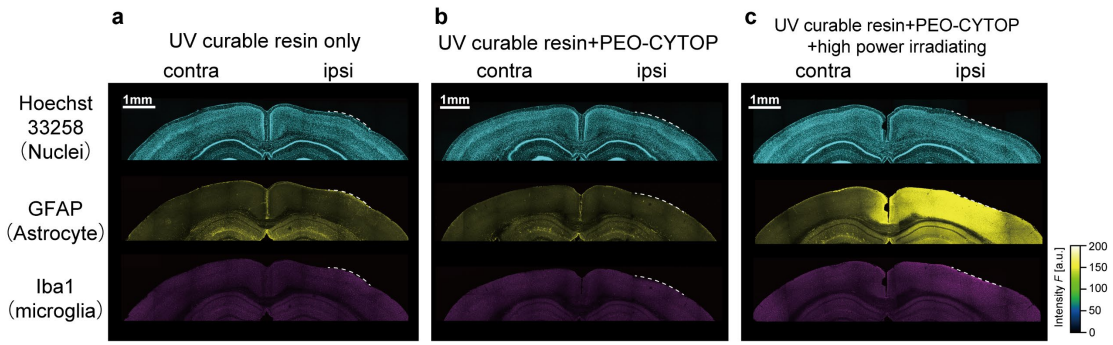

Figure 15 Evaluation of Inflammation in the Brain Tissue in the NIRE Method

a. Immunostaining of Hoechst 33258, GFAP, and Iba1 in a mouse with a cranial window using UV curable resin only (without PEO-CYTOP nanosheet) in optimal irradiating condition at 4 weeks after surgery.

b. Immunostaining of Hoechst 33258, GFAP, and Iba1 in a mouse with a cranial window using the NIRE method in optimal irradiating condition at 4 weeks after surgery.

c. Immunostaining of Hoechst 33258, GFAP, and Iba1 in a mouse with a cranial window using the NIRE method with twice the power irradiation of optimal irradiating condition at 4 weeks after surgery.

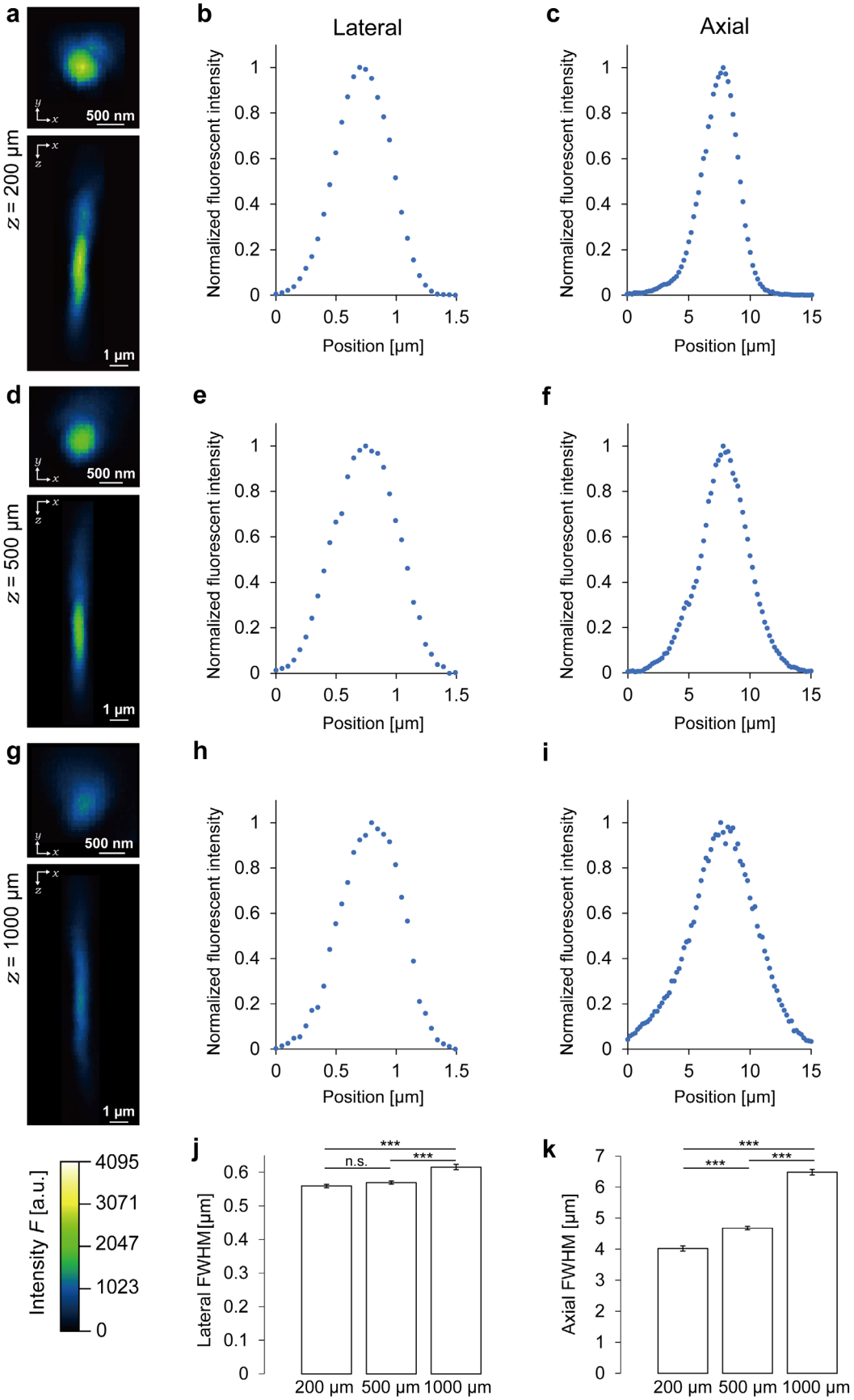
a
b
Lateral
c
Axial
z = 200 µm
500 nm
1 µm
Normalized fluorescent intensity
Position [µm]
d
e
f
z = 500 µm
g
h
i
z = 1000 µm
Intensity F [a.u.]
4095
3071
2047
1023
0
j
Lateral FWHM [µm]
n.s.
***
200 µm
500 µm
1000 µm
k
Axial FWHM [µm]

Figure 16 Evaluation of Spatial Resolution Through the Cranial Window Using the NIRE Method

a. Fluorescent images of 200-nm yellow-green beads obtained through the PEO-CYTOP nanosheet and UV curable resin at a depth of 200 μm in *xy* (top) and *xz* (bottom).

b. Lateral normalized fluorescence intensity of 200-nm yellow-green beads obtained through the PEO-CYTOP nanosheet and UV curable resin at a depth of 200 μm.

c. Axial normalized fluorescence intensity of 200-nm yellow-green beads obtained through the PEO-CYTOP nanosheet and UV curable resin at a depth of 200 μm.

d. Fluorescent images of 200-nm yellow-green beads obtained through the PEO-CYTOP nanosheet and UV curable resin at a depth of 500 μm in *xy* (top) and *xz* (bottom).

e. Lateral normalized fluorescence intensity of 200-nm yellow-green beads obtained through the PEO-CYTOP nanosheet and UV curable resin at a depth of 500 μm.

f. Axial normalized fluorescence intensity of 200-nm yellow-green beads obtained through the PEO-CYTOP nanosheet and UV curable resin at a depth of 500 μm.

g. Fluorescent images of 200-nm yellow-green beads obtained through the PEO-CYTOP nanosheet and UV curable resin at a depth of 1000 μm in *xy* (top) and *xz* (bottom).

h. Lateral normalized fluorescence intensity of 200-nm yellow-green beads obtained through the PEO-CYTOP nanosheet and UV curable resin at a depth of 1000 μm.

i. Axial normalized fluorescence intensity of 200-nm yellow-green beads obtained through the PEO-CYTOP nanosheet and UV curable resin at a depth of 1000 μm.

j. The averaged axial FWHMs measured from the intensity profiles of the beads images obtained from each depth of 200, 500 and 1000 μm; *: $p < 0.05$; **: $p < 0.01$; ***: $p < 0.005$ (Welch's t-test with Bonferroni correction). Error bars represent standard error of the mean.

k. The averaged lateral FWHMs measured from the intensity profiles of the beads images obtained from each depth of 200, 500 and 1000 μm; *: $p < 0.05$; **: $p < 0.01$; ***: $p < 0.005$ (Welch's t-test with Bonferroni correction). Error bars represent standard error of the mean.

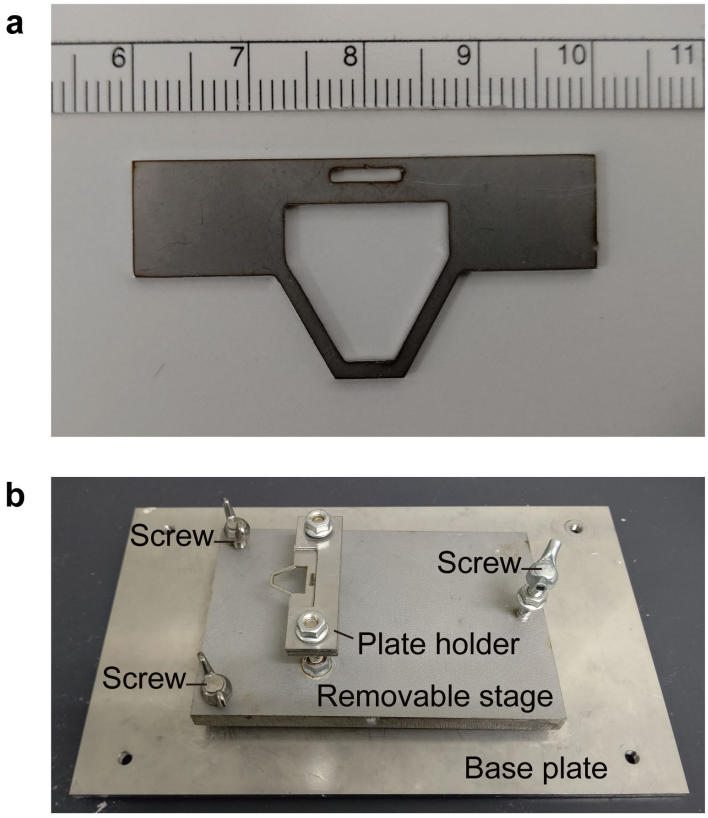

Figure 17 Head-Fix System for *In Vivo* Imaging of Awake Mice

a. The aluminum head plate with the large trapezoidal hole for fixation with a scale ruler (1 mm increments)

b. The newly-developed head-fix system with a horizontal adjustment mechanism to fix the head of the mouse under two-photon microscopy. The head plate was mounted to the plate holder on the removable stage. Three screws are located on the removable stage, the tip of which is fitted to the base plate. The stage angle could be manually controlled by the screws to ensure that the surface of the cranial windows and objective lens were parallel, which would reduce optical aberrations.

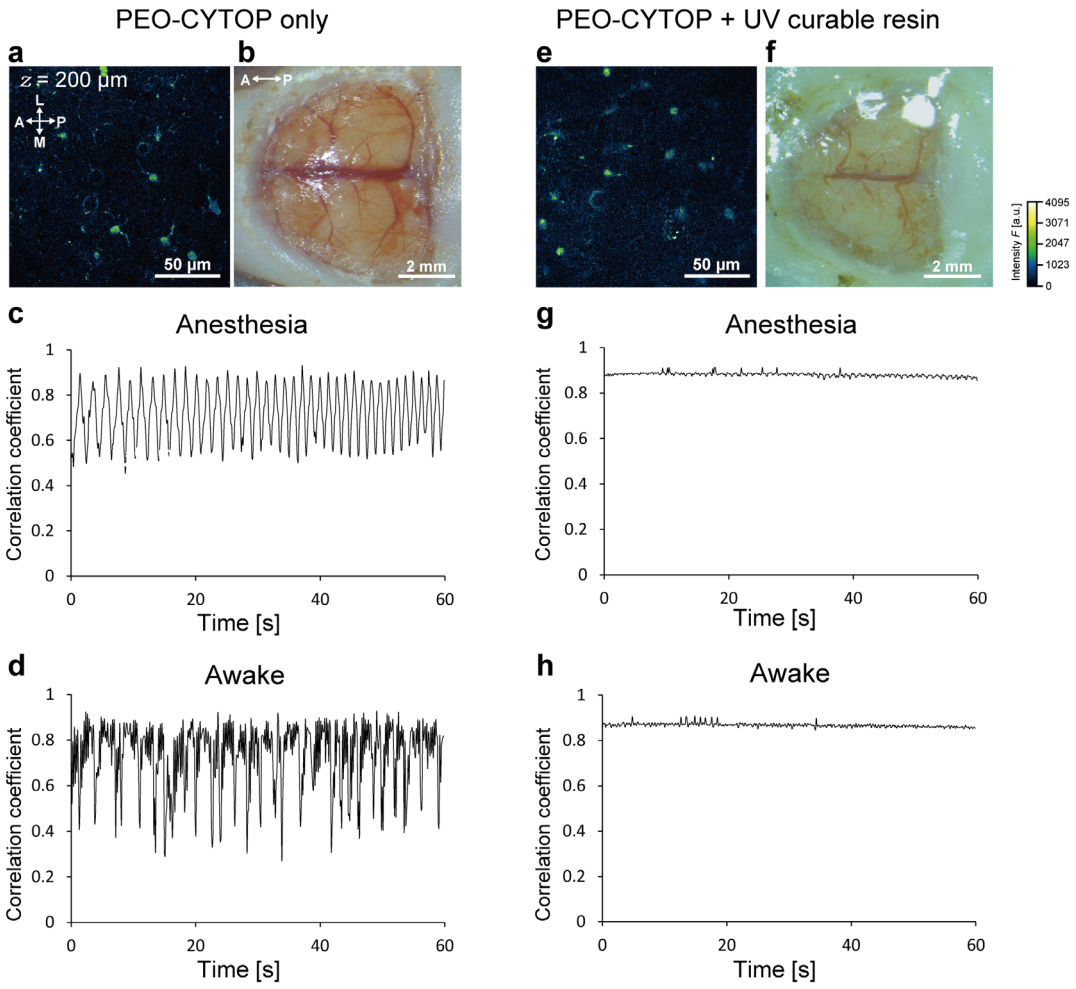

Figure 18 Evaluation of Motion Artifacts in Awake Mice Through the Cranial Window Using the NIRE Method

a. An example image of two-photon imaging of astrocytes labeled with SR101 through the cranial window using a PEO-CYTOP nanosheet. The directions are indicated as anterior (A), posterior (P), medial (M), and lateral (L).

b. The cranial window using a PEO-CYTOP nanosheet on the V1 area in the brain of an adult wild-type mouse.

c. Time series of a correlation coefficient calculated from each frame in the anesthetized condition of the same mouse as Figure 18a.

d. Time series of a correlation coefficient calculated from each frame in the awake condition of the same mouse as Figure 18a.

e. An example image of two-photon imaging of astrocytes labeled with SR101 through the cranial window using a PEO-CYTOP nanosheet and UV curable resin.

f. The cranial window using a PEO-CYTOP nanosheet and UV curable resin on the V1 area in the brain of the same mouse as Figure 18b.

g. Time series of a correlation coefficient calculated from each frame in the anesthetized condition of the same mouse as Figure 18e.

h. Time series of a correlation coefficient calculated from each frame in the awake condition of the same mouse as Figure 18e.

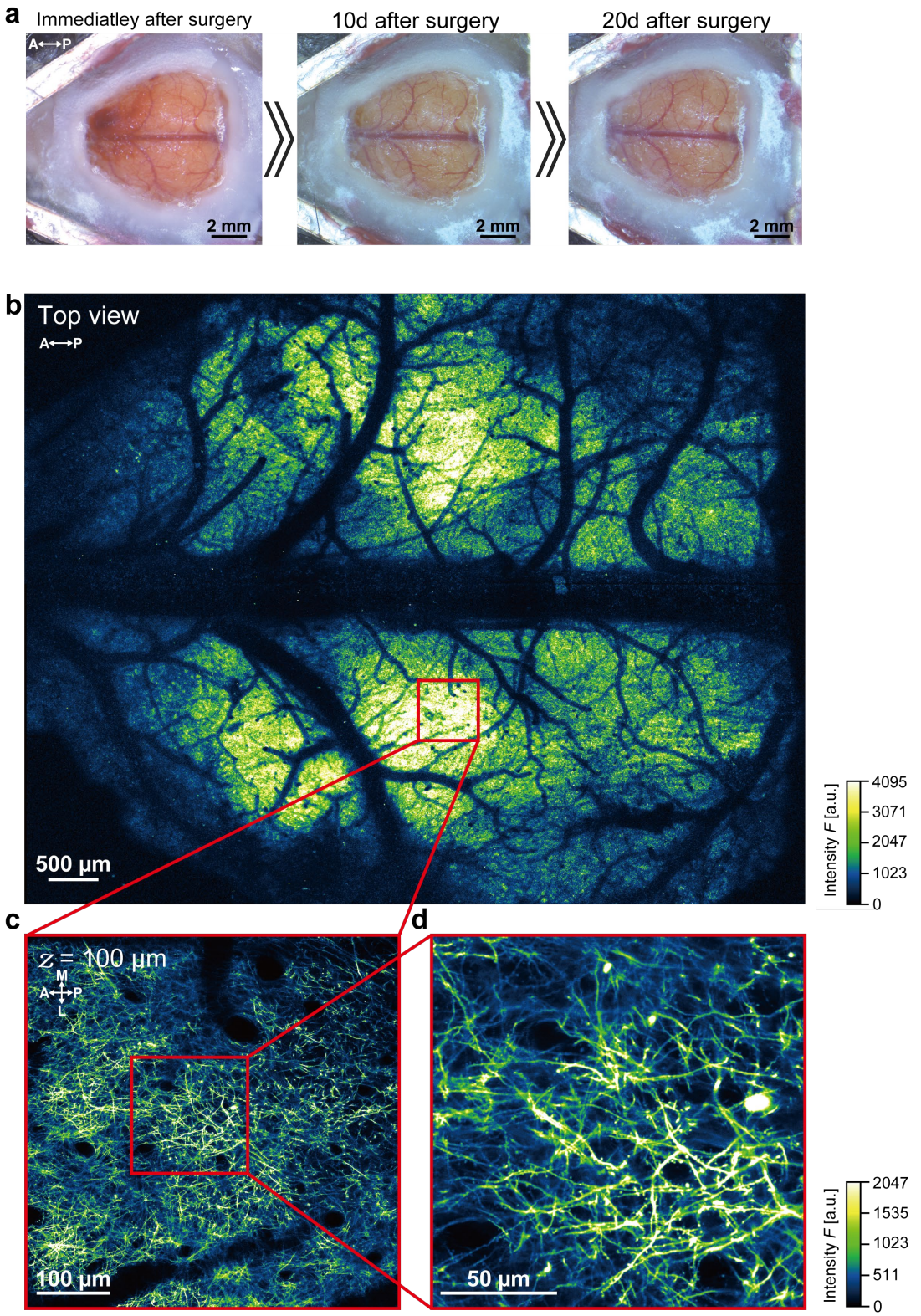

Figure 19 ***In Vivo*** **Multi-Scale Two-Photon Imaging in Thy1-EYFP-H Mice with a**

Cranial Window Using the PEO-CYTOP Nanosheet and UV Curable Resin

a. Time-lapse photos of the large cranial window using the PEO-CYTOP nanosheet and UV curable resin in an H-line mouse. The directions are indicated as anterior (A), posterior (P).

b. Wide-field (~7.8 mm × ~6.0 mm) images tiled with the maximum intensity projections of six three-dimensional stacks through the cranial window in the right photo of Figure 19a. The red box corresponds to the region of Figure 19c. The directions are indicated as anterior (A), posterior (P).

c. Cross-sectional *xy*-images of the axons and apical dendrites from the region located at a depth of 100 μm from the surface indicated as the red box in Figure 19b. The directions are indicated as anterior (A), posterior (P), medial (M), and lateral (L). The red box corresponds to the region of Figure 19d.

d. Cross-sectional *xy*-images of the axons and dendrites with dendritic spines from the region indicated as the red box in Figure 19c.

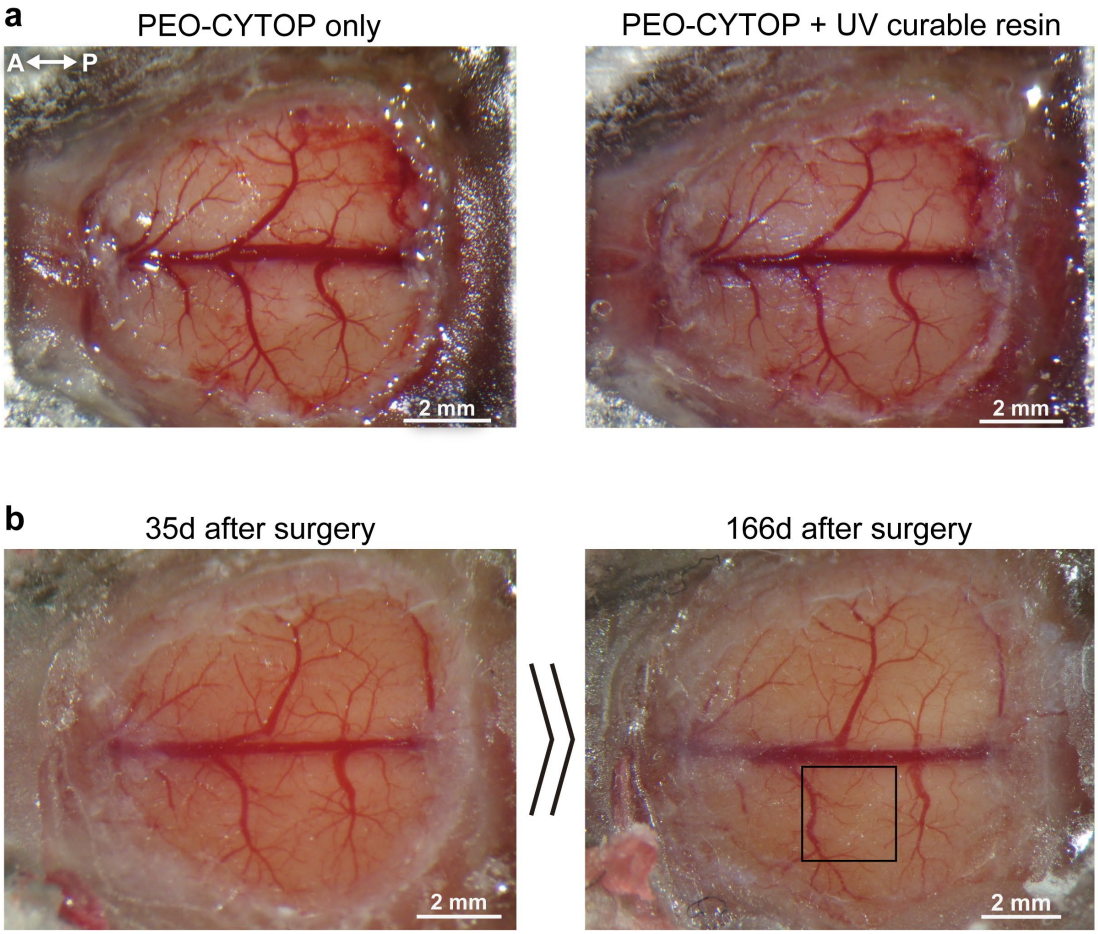

Figure 20 The Transparency of the Large-Scale Cranial Window Using the NIRE Method

a. Photos of the large cranial window before and after curing UV curable resin on the PEO-CYTOP nanosheet immediately after surgery. The directions are indicated as anterior (A), posterior (P).

b. Photos of the cranial window in Figure 20a after 35 days and 166 days from the day of the surgery, respectively. The black box corresponds to the region of Figure 21a.

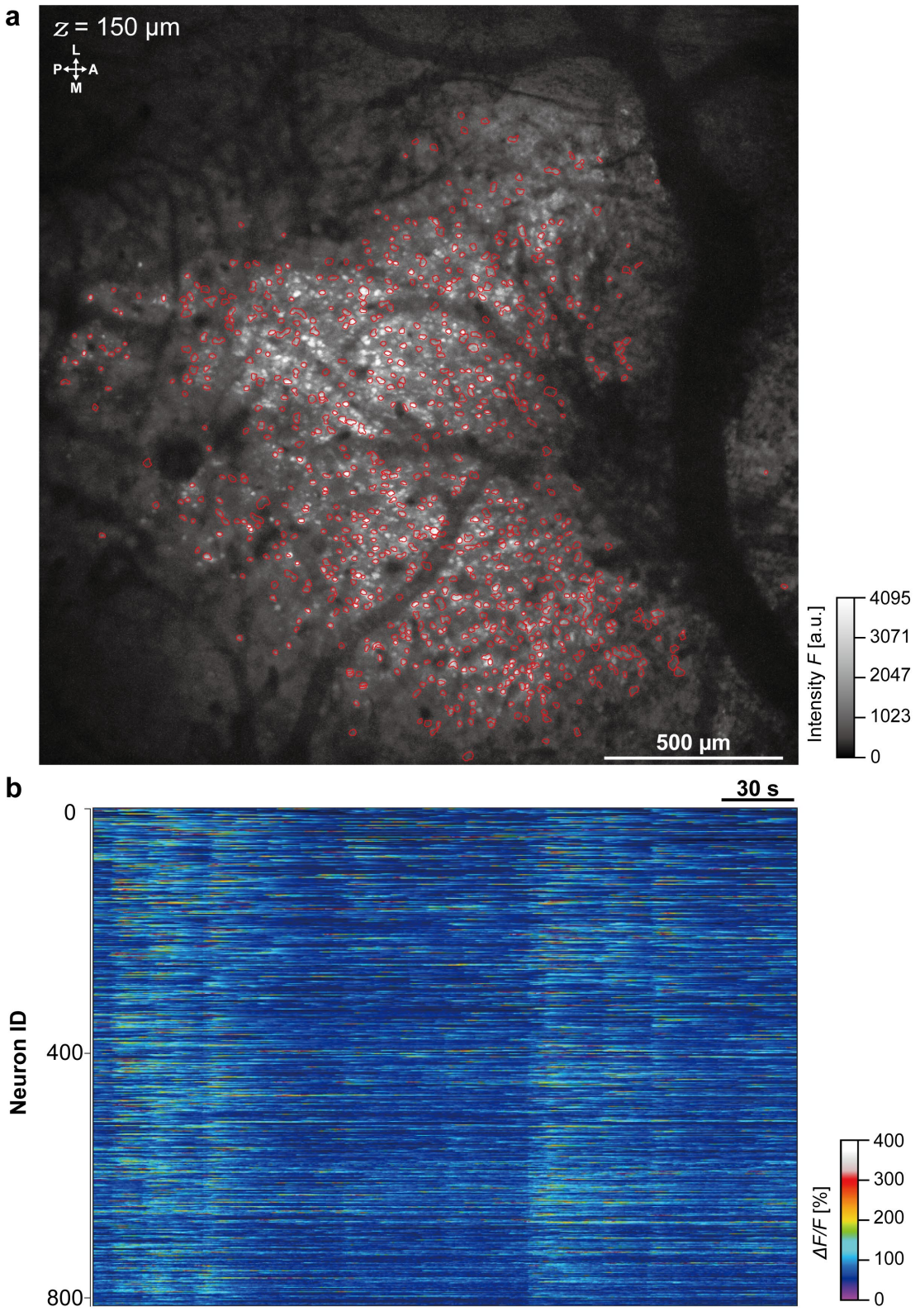

Figure 21 ***In Vivo*** **Large-Scale Calcium Imaging of Neurons with the Cranial**

Window Using the NIRE Method

a. Wide-field (~2.1 mm × ~2.1 mm) images calculated by the maximum intensity projection of time-lapse Ca^{2+} imaging data for 5 minutes obtained from the region indicated as the black box in Figure 20b. The red circles indicate the ROIs for Figure 21b. The directions are indicated as the anterior (A), posterior (P), medial (M), and lateral (L).

b. Heatmap showing the extracted neuronal traces of fluorescence intensity change in 806 neurons identified using the CNMF algorithm (*see* Materials and Methods).

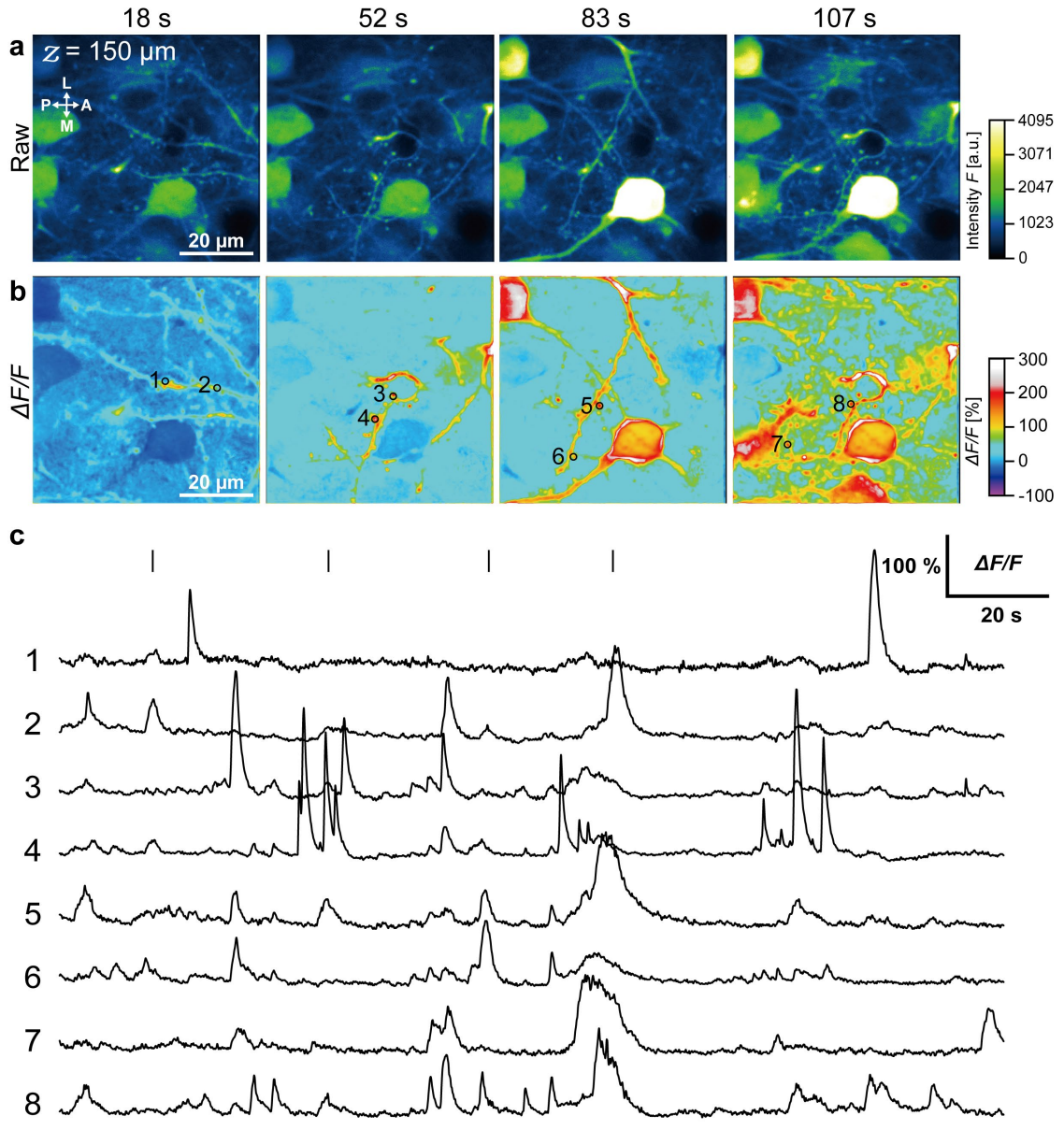

Figure 22 ***In Vivo*** **Calcium Imaging of Soma, Dendrite, and Spines with the Cranial Window Using the NIRE Method**

a. Time-lapse fluorescent images of Ca^{2+} elevations in the mouse of Figure 20. The times are corresponded to each image of Figure 22a and b and are indicated using short solid lines in Figure 22c. The directions are indicated as anterior (A), posterior (P), medial (M), and lateral (L).

b. Time-lapse images of fluorescence intensity changes (*ΔF/F*) calculated by the data

of Figure 22a. The black circles and numbers represent the ROIs for fluorescence intensity traces in Figure 22c.

c. *ΔF/F* traces from the ROIs of Figure 22b. The short solid lines indicate the time of Figure 22b.

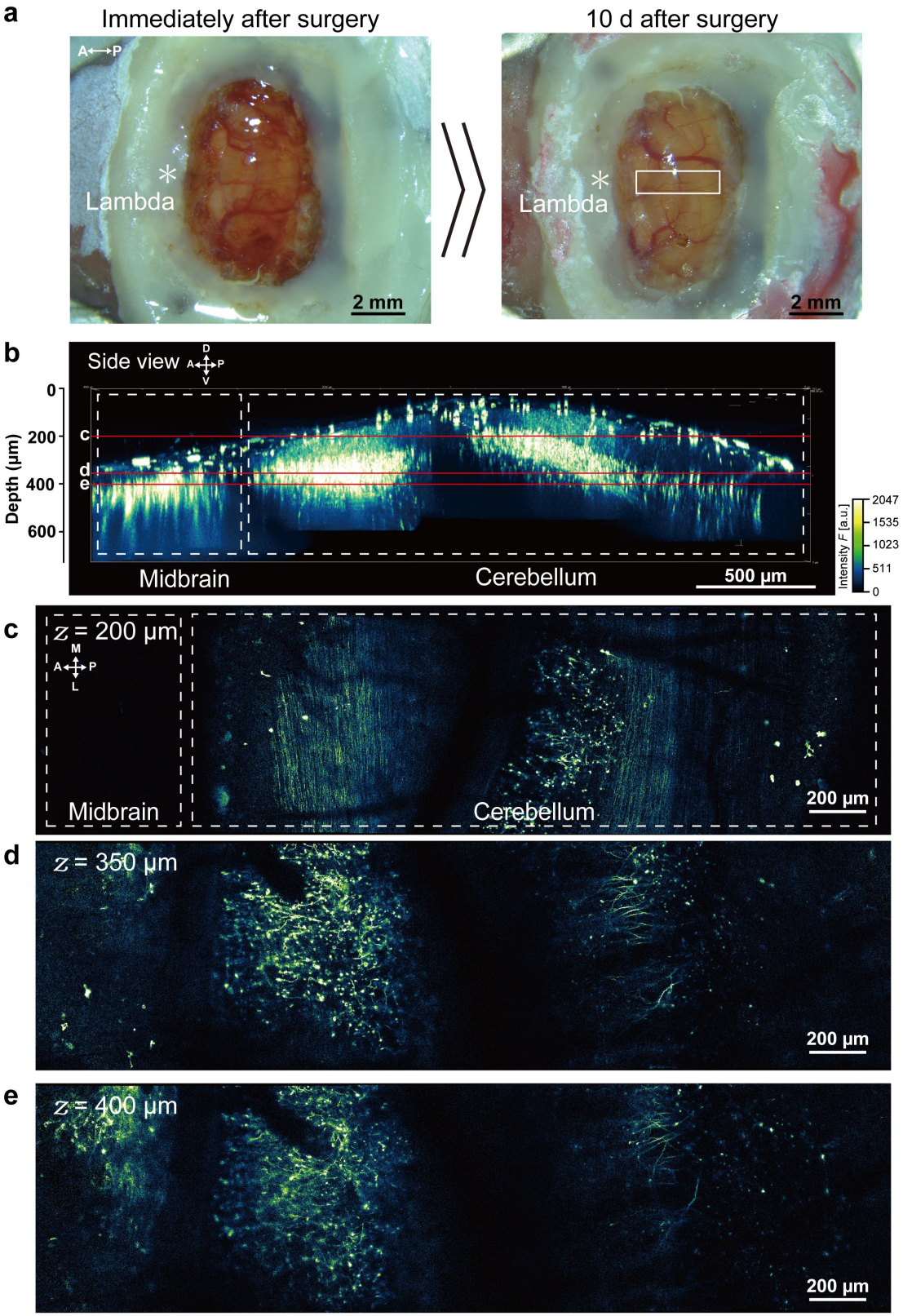

Figure 23 ***In Vivo*** **Two-Photon Imaging of the Cranial Window from the Midbrain**

to the Cerebellum in the NIRE Method

a. Time-lapse photos of the large cranial window covering the cerebellum and midbrain with the PEO-CYTOP nanosheet and UV curable resin in an H-line mouse. The regions within the white boxes correspond to the region of Figure 23b and c. Asterisk indicates the position of lambda. The directions are indicated as anterior (A), posterior (P).

b. Side view of tomographic images tiled with the maximum intensity projections of four three-dimensional stacks in the region shown as the white box in Figure 23a. The dotted boxes roughly correspond to the region of the cerebellum and midbrain. The red lines indicate the section of Figure 23c-e. The directions are indicated as dorsal (D), ventral (V), anterior (A), and posterior (P).

c. Cross-sectional *xy*-images (~ 3.0 mm × ~ 0.8 mm) of the axons or apical dendrites from the region located at a depth of 200 μm from the surface shown as the white box in Figure 23a. The dotted boxes roughly correspond to the region of the cerebellum and midbrain. The dotted line indicates the invisible area under blood vessels. The directions are indicated as anterior (A), posterior (P), medial (M), and lateral (L).

d. Cross-sectional *xy*-images (~ 3.0 mm × ~ 0.8 mm) of the axons or apical dendrites from the region located at a depth of 350 μm from the surface shown as the white box in Figure 23a.

e. Cross-sectional *xy*-images (~ 3.0 mm × ~ 0.8 mm) of the axons or apical dendrites from the region located at a depth of 400 μm from the surface shown as the white box in Figure 23a.

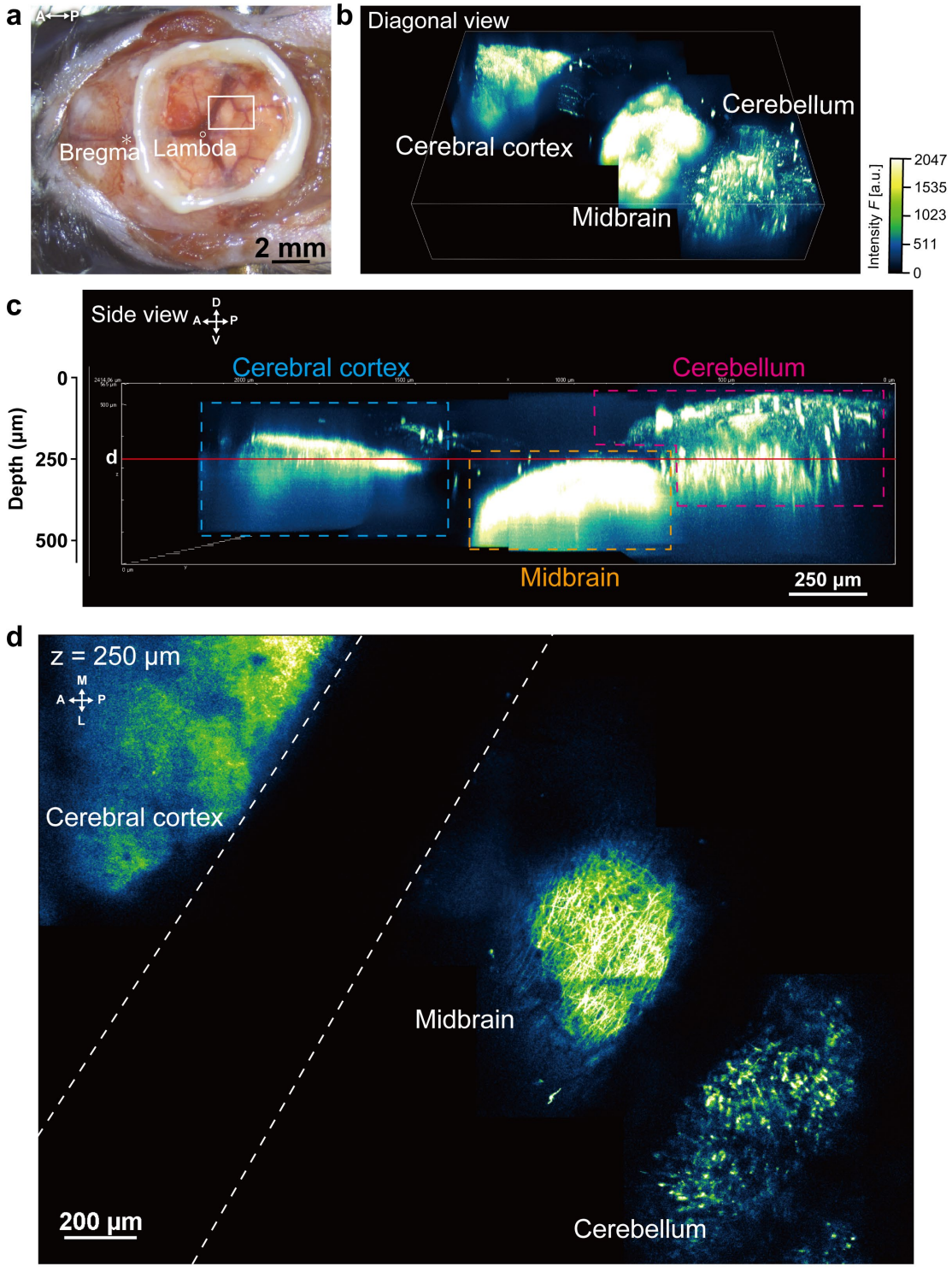

Figure 24 ***In Vivo*** **Two-Photon Imaging of the Large Cranial Window from the Cerebral Cortex to Cerebellum in the NIRE Method**

a. Photo of the large cranial window covering from the cerebral cortex to the

cerebellum with the PEO-CYTOP nanosheet and UV curable resin in an H-line mouse. The regions within the white boxes correspond to the region of Figure 24b-d. Asterisk and white circle indicated each position of bregma and lambda. The directions are indicated as anterior (A), posterior (P).

b. Diagonal view of tomographic images tiled with the maximum intensity projections of the three-dimensional stacks in the region shown as the white box in Figure 24a. The magenta, orange, and cyan dotted boxes roughly correspond to each region of the cerebellum, the midbrain, and the cerebral cortex, respectively.

c. Side view of tomographic images tiled with the maximum intensity projections of the three-dimensional stacks as a coronal section shown as the white box in Figure 24a. The dotted boxes roughly correspond to the region of the cerebellum and midbrain. The red lines indicate the section of Figure 24d. The directions are indicated as dorsal (D), ventral (V), anterior (A), and posterior (P).

d. Cross-sectional *xy*-images (~ 2.4 mm × ~ 1.7 mm) of the region from the cerebellum to the cerebral cortex at a depth of 250 μm from the surface indicated as the white box in Figure 24a. The dotted line indicates the invisible area under blood vessels. The directions are indicated as anterior (A), posterior (P), medial (M), and lateral (L).

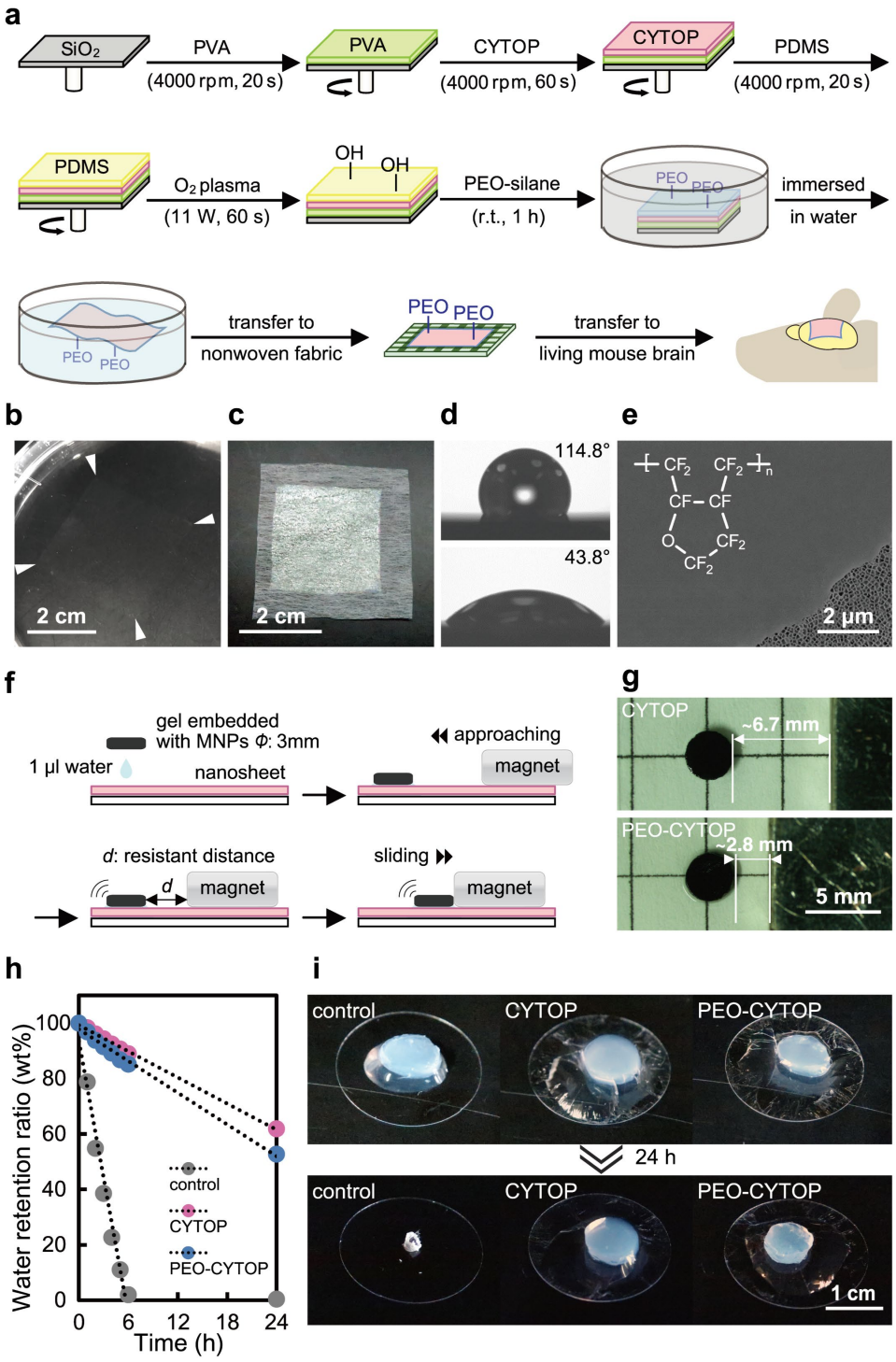

Figure S1 Fabrication and Characterization of the PEO-CYTOP Nanosheet.

a, Schematic representation of the fabrication of a freestanding PEO-CYTOP nanosheet re-supported on a nonwoven fabric for wrapping the living mouse brain.

b, Image of a PEO-CYTOP nanosheet with a thickness of ~130 nm floating on the

surface of the water (the arrows indicate the corner of the nanosheet).

c, Image of a ~130 nm PEO-CYTOP nanosheet re-supported on a nonwoven fabric with the hydrophilic side facing outward.

d, Static water contact angle of the hydrophobic and hydrophilic sides of the PEO-CYTOP nanosheet.

e, SEM image of a PEO-CYTOP nanosheet adhered onto an Anodisc membrane.

f, Schematic representation showing the evaluation of the adhesion capability of the nanosheet using a magnet-driven method.

g, Images captured at the moment at which a magnetic nanoparticle(MNP)-loaded hydrogel overcomes the maximum friction, to be dragged over the CYTOP and PEO-CYTOP nanosheets, respectively.

h, The correlation between the water retention ratio and the time of the test using the CYTOP and PEO-CYTOP nanosheet-wrapped hydrogels.

i, Photos of the hydrogels wrapped with the CYTOP and PEO-CYTOP nanosheets (without nanosheet wrapping as a control) after 24 h.

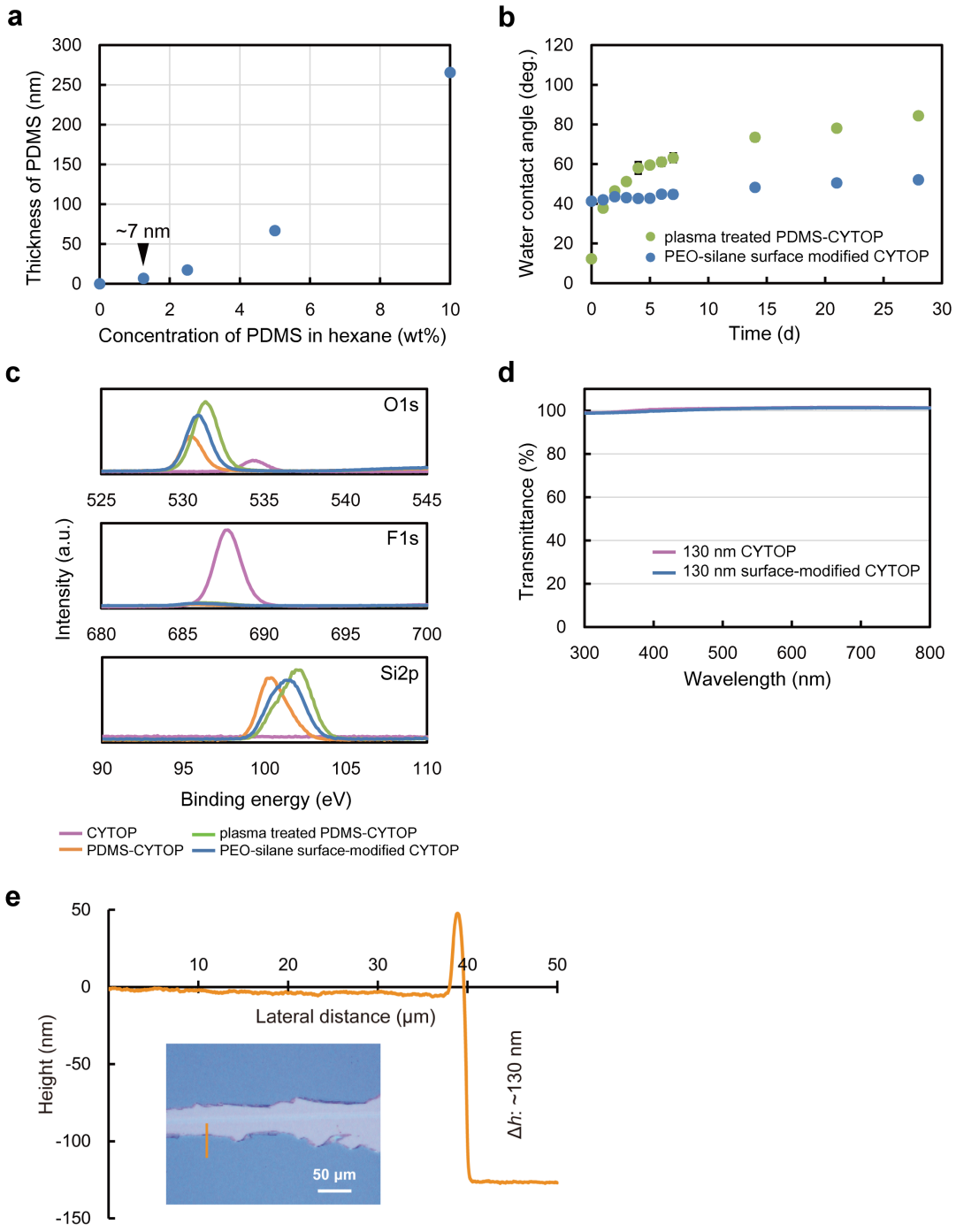

Figure S2 Additional Characterizations of PEO-CYTOP Nanosheet.

a, The thickness of the PDMS layer coated on the surface of the CYTOP versus the concentration of PDMS in hexane for spin casting.

b, The static water contact angle of the plasma-treated PDMS-CYTOP nanosheet and

the PEO-silane surface-modified CYTOP nanosheet during 1 month continuous observation.

c, X-ray photoelectron spectroscopy results of the surfaces of pristine CYTOP, PDMS-CYTOP, plasma-treated PDMS-CYTOP, and the PEO-silane surface-modified CYTOP nanosheet.

d, Transmittance in the wavelength from 300 to 800 nm of the CYTOP and PEO-CYTOP nanosheets with a similar thickness of ~130 nm.

e, Characterization of thickness using a stylus profilometer. Inset was the optical image of the scratching groove on the nanosheet made with a scalpel, and the orange line indicates the location of the moving stylus. The thickness of the nanosheet was determined from the average height difference between the surface of the nanosheet and the silicon wafer.